

1 Photochemical and ozone-induced aging significantly alter the 2 viscosity of aqueous *trans*-aconitic acid aerosol particles

3 Cynthia Antossian¹, Marcel Müller^{1,a}, and Ulrich K. Krieger¹

4 ¹Institute for Atmospheric and Climate Science, ETH Zurich, Universitätstrasse 16, 8092 Zurich, Switzerland

5 ^acurrently at: Institute of Biogeochemistry and Pollutant Dynamics, ETH Zurich, Universitätstrasse 16, 8092
6 Zurich, Switzerland

7
8 Correspondence to: Ulrich K. Krieger (ulrich.krieger@env.ethz.ch) and Cynthia Antossian
9 (cynthia.antossian@env.ethz.ch)

10 **Abstract.** Aging processes of organic aerosols, including reactions with gas phase oxidants, such as ozone (O₃),
11 as well as photochemical reactions, can significantly alter their physicochemical properties. While previous
12 research has examined how photochemical aging and ozonolysis affect the physicochemical properties of organic
13 aerosols, our study investigates the combined effect of photolysis and ozonolysis. We use aqueous *trans*-aconitic
14 acid as a proxy for secondary organic aerosol particles (SOA), selected for its ability to absorb UV light and for
15 containing a C=C double bond that is susceptible to ozonolysis. We observe significant mass loss in single particles
16 levitated in an electrodynamic balance when exposed to either O₃ or UV light (375 nm), as well as to both aging
17 processes simultaneously, resulting from fragmentation reactions followed by the volatilization of some of the
18 products. Viscosity measurements at 17% relative humidity revealed an increase of nearly 4 orders of magnitude
19 after both UV exposure and combined UV and O₃ exposure at 60% mass loss. Interestingly, continued UV-aging
20 beyond 60% mass loss resulted in a viscosity decrease, whereas combined UV and O₃ exposure led to a further
21 viscosity increase. Hygroscopicity exhibited only a modest decline after 20% mass loss during UV-aging and
22 remained constant with further UV exposure; this reduction was less pronounced when UV-aging occurred in the
23 presence of O₃. Overall, our results indicate that the mixing times within accumulation mode SOA particles may
24 increase from 4 s to 4 h after aging under dry boundary layer conditions.

25 26 1 Introduction

27 Aerosol particles play a prominent role in the atmosphere, since they are involved in many important processes
28 including cloud formation, biogeochemical cycling, and light scattering (Seinfeld and Pandis, 2016). Moreover,
29 aerosols affect human health, since they have been associated with respiratory and cardiac diseases, oxidative
30 stress, and cancer (Dockery and Pope, 1994; Nel, 2005). Organic compounds constitute a major fraction of
31 atmospheric aerosols (20-90%) (Kanakidou et al., 2005; Jimenez et al., 2009). A significant fraction of these
32 aerosols are secondary organic aerosols (SOA) (Zhang et al., 2007), which are formed when volatile organic
33 compounds oxidize and produce compounds with low volatility that partition from the gas phase into the particle
34 phase, eventually forming SOA (Pankow, 1994). In addition, these low volatility compounds can partition into
35 preexisting aerosols, leading to internal mixing of primary and secondary aerosol particles (Marcolli et al., 2004;
36 Marcolli and Krieger, 2020)

37 Throughout their lifetimes in the atmosphere, these organic aerosol particles undergo various aging processes. One
38 of these processes are reactions with gas phase oxidants, such as ozone (O₃), hydroxyl radicals (OH), and nitrate
39 radicals (NO₃). In addition to the reactions with oxidants, organic aerosols can undergo photochemical reactions
40 due to exposure to UV or even visible light, either directly or indirectly by photosensitizers, leading to additional
41 aging. Oxidation reactions can occur through different pathways (Kroll and Seinfeld, 2008), depending on the
42 chemical composition of the gas and particle phase and on the atmospheric conditions, such as temperature and
43 relative humidity (RH). For instance, fragmentation can take place because of carbon-carbon double bond
44 cleavage, leading to more volatile products that volatilize from the particle. Functionalization can also take place
45 because of the addition of polar functional groups, thus increasing oxygen-to-carbon ratio O:C and forming more
46 hygroscopic, higher molecular weight products that have low volatility. In addition, oligomerization or accretion
47 can occur through the association of small molecules, consequently forming products with similar O:C, but higher
48 number of carbon atoms that have low hygroscopicity, low volatility, and high viscosity (Kroll and Seinfeld, 2008).
49 Fragmentation reactions have been observed for a range of organic aerosol particles during photochemical aging
50 or when exposed to atmospheric oxidants (O'Brien and Kroll, 2019; Sun and Smith, 2024; Dou et al., 2021; Kroll

51 et al., 2015). Moreover, oxidation of SOA has been shown to induce the formation of oligomers through accretion
52 reactions e.g. Kalberer et al. (2004). At present, it remains uncertain which mechanisms dominate under different
53 aerosol compositions and atmospheric conditions, making it challenging to predict aerosol properties during and
54 after aging.

55 These aging processes can significantly alter the physicochemical properties of organic aerosols, such as the
56 viscosity and hygroscopicity (Hosny et al., 2016; Athanasiadis et al., 2016; Baboomian et al., 2022; Jimenez et al.,
57 2009; Kroll et al., 2011; Kroll et al., 2015). Viscosity of organic aerosols varies over a wide range, depending on
58 the chemical properties, such as molecular structure, functional groups, chain length, molecular weight, and carbon
59 oxidation state and on the environmental conditions, such as temperature and relative humidity (Gou et al., 2025).
60 Moreover, the viscosity of organic aerosols is an indication of the phase state, with aerosols having viscosity values
61 less than 10^2 Pa s considered as being liquid, between 10^2 and 10^{12} Pa s semi-solid, and greater than 10^{12} Pa s solid
62 (Shiraiwa et al., 2011; Koop et al., 2011).

63 Viscosity affects the condensed phase chemistry (Pöschl and Shiraiwa, 2015; Kuwata and Martin, 2012), gas-
64 particle partitioning (Shiraiwa et al., 2011; Zaveri et al., 2014), and the ability of the aerosol particle to act as ice
65 nucleating particles (Wolf et al., 2020; Murray et al., 2010), while hygroscopicity affects the ability of the particle
66 to act as cloud condensation nuclei (Chan et al., 2008), thereby affecting the Earth's energy budget and climate.
67 Moreover, viscosity affects the ability of the particle to react with other chemical species. Viscous aerosols can
68 limit molecular motion due to slow diffusion of oxidants, water, and organic compounds (Pöschl and Shiraiwa,
69 2015). This makes particulate air pollutants less susceptible to degradation and increases their mixing times in the
70 troposphere, thereby favoring their transport and affecting human health (Mu et al., 2018; Bastelberger et al., 2017).
71 For instance, polycyclic aromatic hydrocarbons (PAHs) that were coated with viscous organic aerosols, were
72 shielded from oxidation, highlighting stronger long-range transport and elevated lung cancer risk (Shrivastava et
73 al., 2017; Zelenyuk et al., 2012).

74 Several studies have observed the change in viscosity of organic aerosols upon aging. For instance, studies on the
75 ozonolysis of oleic acid aerosols (Hosny et al., 2016) and squalene droplets (Athanasiadis et al., 2016) indicate a
76 significant increase in viscosity upon oxidation. SOA formed from ozonolysis of organic aerosols might also
77 undergo additional aging, for instance photochemically, altering further the viscosity of these particles. A recent
78 study on the photochemical aging of SOA generated from the ozonolysis of d-limonene and α -pinene shows an
79 increase of several orders of magnitude in viscosity after UV-aging, ultimately transforming into a glassy solid
80 state, especially at low temperatures and low relative humidities (Baboomian et al., 2022). However, to the best of
81 our knowledge, it is not known how the aerosol properties, particularly viscosity and hygroscopicity, will change
82 after simultaneous exposure to UV light and ozone, as simultaneously encountered in Earth's atmosphere during
83 daytime.

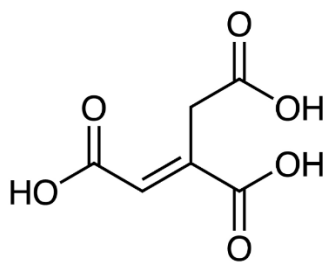
84 In this work, we use *trans*-aconitic acid particles as surrogate for SOA to investigate how the viscosity and
85 hygroscopicity are influenced by different degrees and different combinations of photochemical and ozone-induced
86 aging.

87

88 **2 Materials, Instrumentation, and Method**

89 **2.1 Materials**

90 *Trans*-aconitic acid (AA) is a naturally occurring tricarboxylic acid that is produced by several plants and
91 accumulates significantly in sugar cane and sweet sorghum (Bruni and Klasson, 2022). Since it is a highly oxidized
92 molecule having carboxyl functional groups, it has low vapor pressure, and is water soluble, we use it here as a
93 proxy system for SOA present in the atmosphere.



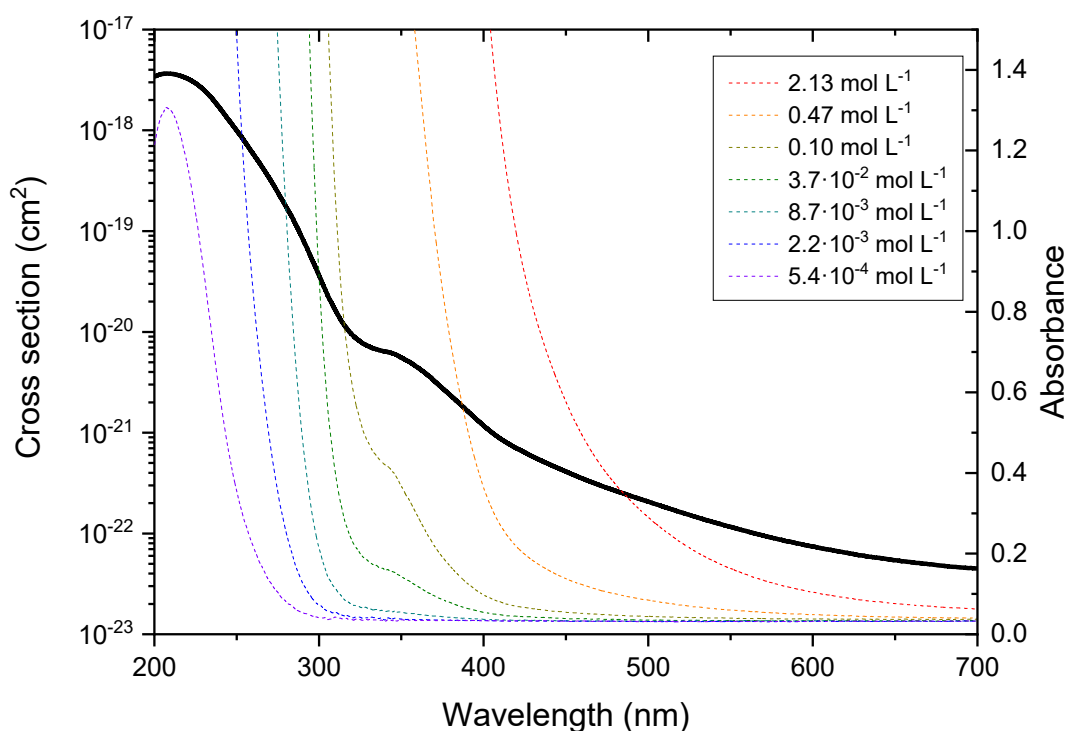
94

95 **Figure 1: The structure of *trans*-aconitic acid.**

96 The UV-visible absorption spectra (Fig. 2) obtained using a UV-Visible spectrophotometer (Varian Cary 100 Bio)
 97 shows that concentrated AA solution (2.13 mol L^{-1}) absorbs even in the visible range of the solar spectrum, with
 98 significant absorbance at 375 nm. AA's absorbance at the visible to near UV wavelengths could be attributed to
 99 the conjugated structure of *trans*-aconitic acid, which makes it possible to undergo photochemical reaction at 375
 100 nm illumination. However, it should be noted that AA (98%, Sigma Aldrich) was used without any further
 101 purification, and it is known that the presence of even trace amounts of impurities can affect UV absorption (Saito
 102 et al., 2023). Further investigation is needed to clarify the origin of the observed absorption.

103 In comparison to 4-nitrocatechol, a typical brown carbon chromophore, the cross section of *trans*-aconitic acid is
 104 about 3 orders of magnitude lower between 300 and 600 nm (Cornard et al., 2005). Moreover, the presence of the
 105 double bond makes AA susceptible to ozonolysis. As a result of all these properties, AA was chosen in this study
 106 as a suitable proxy system for SOA for studying possible synergistic effects between photochemistry and
 107 ozonolysis.

108



109

110 **Figure 2: Absorption spectra (colored lines) and cross section (black line) of AA solution of different concentrations as**
 111 **a function of wavelength (absorbance values higher than 1.5 are not shown because they are above the maximum**
 112 **detection limit of the instrument). The cross section was calculated using Beer-Lambert's law, based on the absorbance**
 113 **values of the AA solutions.**

114

115

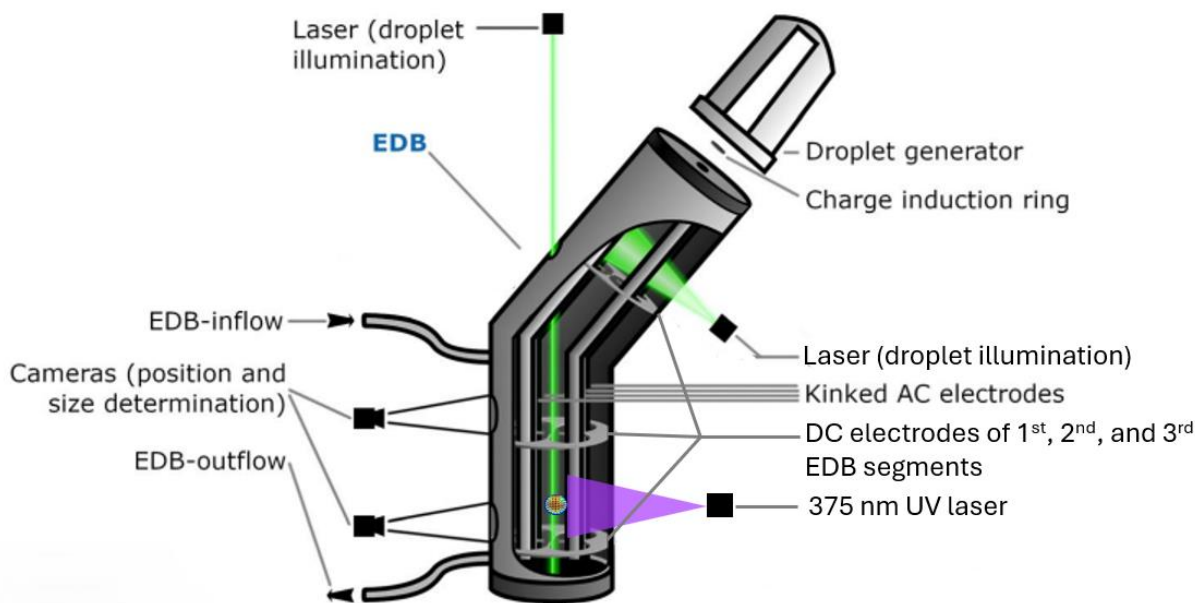
116 2.2 Electrodynamic Balance Setup

117 Experiments on single, levitated, aqueous AA particles were conducted using a linear electrodynamic balance
118 (EDB) (Fig. 3). The set-up has been described previously (Müller et al., 2022). Briefly, single aqueous AA droplets
119 were prepared from 4 wt-% AA in Milli-Q water and injected using a droplet on demand generator (HP-inkjet
120 cartridge model 51604). The droplet was inductively charged and levitated in the EDB trap by AC and DC electric
121 fields. 50 sccm of humidified flow from hydrocarbon free synthetic air (PanGas, 20% O₂ in N₂) was used to keep
122 RH in the EDB at 78% – 88%. The radius of the particles after equilibration to RH was in the range 10–20 µm. All
123 experiments were performed at room temperature (~298 K). RH and temperature were measured using two sensors
124 (Sensirion SHT85, Switzerland) placed at the flow entrance to the EDB as well as at the flow exit of the EDB. The
125 sensor at the flow exit is located close to the levitated particle and it was confirmed in measurements of the
126 deliquescence RH of NaCl particles that this sensor's RH readout is close to the RH at the location of the particle.
127 The uncertainty in RH measurement is ± 1.5%.

128 Aging experiments were conducted by exposing liquid AA particles to 10 ppm ozone generated by UV photolysis
129 of O₂ in synthetic air using an ozone generator (AOS, BMT Messtechnik, Germany). The readout of an
130 electrochemical ozone sensor (OX-B431 on Alphasense ISB, Alphasense, UK) was used to control the ozone
131 generator. For UV exposure, the unfocused beam of a 375 nm UV laser (Omicron LuxX-20, Germany) illuminated
132 the particle levitated at the second segment of the EDB. Its beam profile and power lead to an irradiance at the
133 particle location of about $(1.0 \pm 0.3) \text{ W cm}^{-2}$.

134 The O₃ exposure used in the experiments is similar to an atmospheric exposure of 100 ppb ozone for 10 d, which
135 is a typical lifetime of atmospheric aerosols. The UV photon flux used in the experiments is a factor of 60 larger
136 than atmospheric conditions, based on the power density of the laser irradiation and AA absorbance together with
137 the solar irradiance integrated over the entire spectrum.

138 The particle was illuminated with a 532 nm diode pumped solid state laser (Thorlabs, DJ532, USA) and the
139 scattered light was collected on CCD cameras (Raspberry Pi HQ camera, UK). The change in mass of the particle
140 was deduced by measuring the electric force needed to balance the gravitational force of the particle. The DC
141 voltage was adjusted by an automatic feedback loop driven by the particle image. Since in addition to the
142 gravitational force, the DC voltage compensates for the Stokes force of the gas flow, drag force correction was
143 applied to deduce changes in mass. The drag force was measured by setting the gas flow to 0 sccm and recording
144 the DC voltage that needs to be applied to keep the particle levitated. Based on the difference between the DC
145 voltage at 50 sccm and 0 sccm, the drag force was deduced for the specific size of the particle at the time of
146 measurement. Moreover, the size of the particle was deduced from the two-dimensional angular optical scattering
147 (TAOS) pattern of laser-illuminated droplets. The inverse of the fringe distance along the symmetry axis of the
148 TAOS pattern is a direct measure of the size; smaller size changes are detected by following a single maximum in
149 the TAOS pattern. Thus, the radius of the particle was deduced from the mean distance between the fringes as long
150 as the particle remained spherical and symmetric with regular TAOS pattern. For detecting phase transitions
151 breaking the spherical symmetry of the particle, we use the pattern distortion parameter as introduced by Braun
152 and Krieger (2001). More details on the radius retrieval can be found in Appendix A.

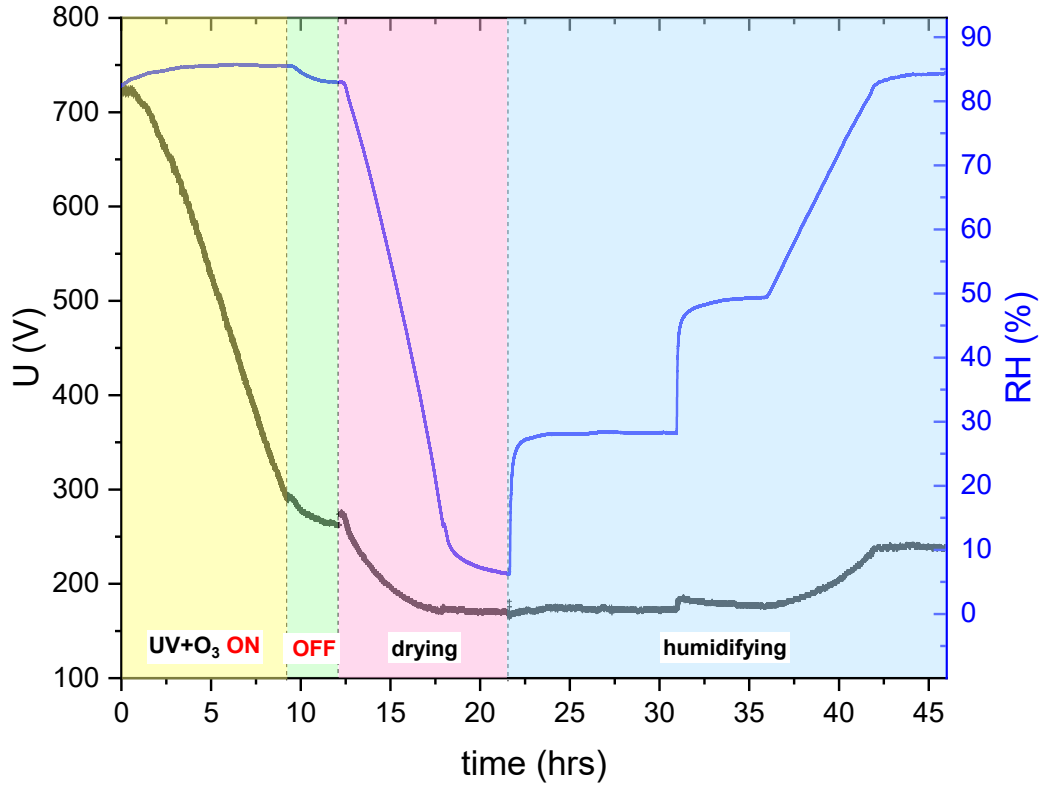


153

154 **Figure 3: Schematic representation of the EDB set-up, adopted with slight modifications from Müller et al. (2022). The**
 155 **UV laser illuminated the particle levitated at the 2nd segment of the EDB. For simplification and better representation,**
 156 **the UV laser was shown in this figure in the 3rd segment of the EDB.**

157 **2.3 Overview of the experimental procedure**

158 Figure 4 shows an example of the experimental procedure to obtain hygroscopicity as well as viscosity for a
 159 combined ozonolysis and photochemical aging experiment. Initially, an aqueous AA particle is injected and
 160 levitated in the EDB. After RH is equilibrated at ~83%, 375 nm UV laser and 10 ppm O₃ are switched on (t=0).
 161 The change in mass is monitored and size measurements are done in parallel. The reaction is carried out at
 162 approximately constant RH, and UV illumination and O₃ are switched off after the particle loses 60% of its initial
 163 mass. Since slight fluctuations in RH and temperature occur after switching off O₃, the particle is kept in the dark
 164 until RH, and therefore the mass and size of the particle are almost constant. Kinetics of the reaction will be
 165 discussed in Sect. 3.2. Afterwards, RH inside the EDB is decreased slowly at a rate of 0.2% min⁻¹ from ~83% to
 166 ~6% and then kept constant for 3.5 h to ensure sufficient drying. From this drying part of the experiment,
 167 hygroscopicity is deduced, as will be explained in more detail in Sect. 2.4. Finally, RH is increased in two steps
 168 rapidly, first from 6.3% to 28.2%, then from 28.2% to 49.4%, and finally raised back from 49.4% to 84.4% slowly.
 169 While the flow change is indeed step-like, the response in RH is approximately exponential. The first step in
 170 humidity was used to derive condensed phase water diffusivity, as will be discussed in more detail in Sect. 2.5.



171
 172 **Figure 4: Overview figure showing the complete experimental procedure of AA particle exposed to UV and O₃**
 173 **simultaneously until 60% mass loss at room temperature. The black line represents the voltage needed to keep the**
 174 **particle levitated in the EDB (corrected for drag force), which is proportional to the mass of the particle. The blue line**
 175 **represents the RH data. The yellow section corresponds to switching on UV laser and O₃, the green section corresponds**
 176 **to turning off UV and O₃, the pink section corresponds to drying, and the blue section corresponds to humidifying.**

177
 178 **2.4 Hygroscopicity measurement**

179 Hygroscopicity and water diffusivity measurements were done on aged particles after they lost about 20%, 40%,
 180 50%, 60% and 80% of their mass. For hygroscopicity measurements, RH was allowed to decrease slowly, at a rate
 181 of 0.2% min⁻¹, by adjusting the ratio of dry nitrogen gas flow relative to the humidified flow while keeping the
 182 total flow constant using automatic mass flow controllers. The change in mass of the particles was monitored
 183 during drying using the automatic feedback loop, see Fig. 4.

184 The hygroscopic size growth factor ($G(RH)$) indicates the relative increase in size of the particles at a certain RH
 185 relative to dry conditions in response to water uptake. If $G(RH)$ is measured at different RH, a single parameter,
 186 κ , for hygroscopic size growth can be determined, assuming ideality (Petters and Kreidenweis, 2007):

187
$$G(RH) = \frac{D(RH)}{D_0} = \left(1 + \kappa \frac{a_w}{1-a_w}\right)^{1/3} \quad (1)$$

188 where $D(RH)$ is the mobility diameter of the particle at a certain RH, D_0 is the diameter of the particle at dry
 189 conditions, and a_w is the water activity, which is equal to RH at equilibrium.

190 Since here the mass growth factor ($g(RH)$) was measured instead of the size growth factor, κ can be determined
 191 from the mass growth factor by using Eq. (2) (Zardini et al., 2008):

192
$$g(RH) = \frac{m(RH)}{m_0} = 1 + ((G(RH))^3 - 1) \frac{\rho_w}{\rho_0} \quad (2)$$

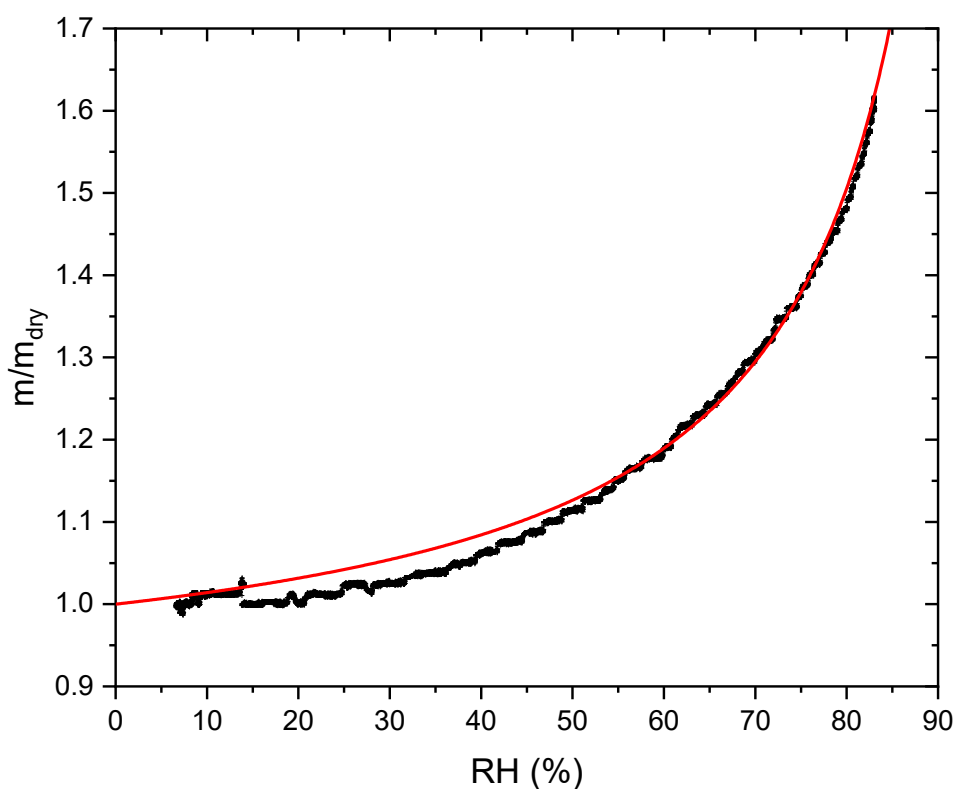
193 Combining Eq. (1) and Eq. (2) yields Eq. 3:

$$194 \quad g(RH) = 1 + \left(\kappa \frac{a_w \rho_w}{1 - a_w \rho_0} \right) \quad (3)$$

195 where $m(RH)$ is the mass of the particle at a certain RH, m_0 is the mass of the particle at dry conditions (measured
196 at ~6% RH), ρ_w is the density of water, and ρ_0 is the density of the particle at dry conditions. ρ_0 for AA was
197 determined experimentally using the conventional additivity rule and was found to be 1.56 g cm^{-3} and was assumed
198 to remain constant after aging, see Appendix B.

199 Since most untreated AA effloresced at RH 59.9%, κ -parametrization fitting according to Eq. (3) was done only in
200 the RH range 62% – 80% for all particles. Furthermore, fitting at higher RH provides a better estimation for κ as
201 deviations from ideality and kinetic limitations to hygroscopic mass transfer become less important with dilution.
202 In addition, we assume that no further chemical processing occurs once UV and O_3 are switched off. Figure 5
203 shows an example of the measured mass growth together with a regression of Eq. (3) to deduce κ .

204



205

206 **Figure 5: Mass growth factor as a function of RH for AA exposed to UV light and O_3 till 60% mass loss (black line). The**
207 **red line is the κ -parametrization fitting in the RH range 62% – 80%, yielding a κ of 0.197.**

208

209 2.5 Viscosity determination

210 Viscosity of the particles after aging was inferred indirectly by estimating the water diffusivity and then using the
211 fractional Stokes–Einstein relation to deduce the viscosity.

212 For water diffusivity measurements, the aged particles were subjected to drying and were kept under low RH
213 (below 15%) for 4 ± 1 h, until RH stabilized around 6%. Then, RH was increased rapidly from $6.7 \pm 0.7\%$ to 28.6
214 $\pm 0.5\%$ and kept constant for 9 ± 2 h. As RH increases, water diffuses from the gas phase into the particle phase
215 until equilibrium between water activity throughout the particle and RH of the gas phase is reached (Koop et al.,

216 2011). The time taken to reach equilibrium depends on the viscosity of the particle, i.e. liquid droplets will reach
 217 equilibrium faster than amorphous solid or glassy particles. Thus, water diffusivity can be inferred by observing
 218 the time response in particle mass or size following a step increase in RH (Zobrist et al., 2011; Bones et al., 2012).
 219 One way of retrieving the diffusion coefficient from such data is by using a numerical model, solving the diffusion
 220 equation (Zobrist et al., 2011; O'Meara et al., 2016). Alternatively, the response of step increase in RH may be
 221 approximated by an exponential approach to the new RH setting, see data and exponential fit in Fig. 6. While a
 222 viscous liquid close to the glass transition exhibits a non-linear response leading to a non-exponential relaxation
 223 (Debenedetti and Stillinger, 2001; Rickards et al., 2015), a less viscous liquid may be reasonably well approximated
 224 by a single exponential response. Under these conditions, the hygroscopic response can be deconvoluted
 225 analytically as detailed in Appendix C. The response $y(t)$ to the hygroscopic 'step' in either mass or size is then
 226 given by Eq. (4) with τ_1 being the characteristic time of the response we are searching for and τ_2 being the
 227 characteristic time of the RH step, induced by the flow change from dry to humidified.

$$228 \quad y(t) = \left(1 - e^{-t/\tau_1}\right) - \frac{\tau_2}{\tau_2 - \tau_1} \left(e^{-t/\tau_2} - e^{-t/\tau_1}\right) \quad (4)$$

229 Water diffusivity can then be approximately deduced from τ_1 using the following equation (Seinfeld and Pandis,
 230 2016; Bones et al., 2012):

$$231 \quad \tau_1 = \frac{r^2}{\pi^2 D} \quad (5)$$

232 where τ_1 is the characteristic time, r is the radius of the particle, and D is the diffusion coefficient.

233 We show in Appendix D that this linear response approximation needs a correction to obtain D , such that it
 234 compares favorably with a full numerical model for water diffusivities in the range of $1.7 \times 10^{-12} \text{ cm}^2 \text{ s}^{-1}$ to 2×10^{-9}
 235 $\text{cm}^2 \text{ s}^{-1}$ and particle sizes used in our experiment.

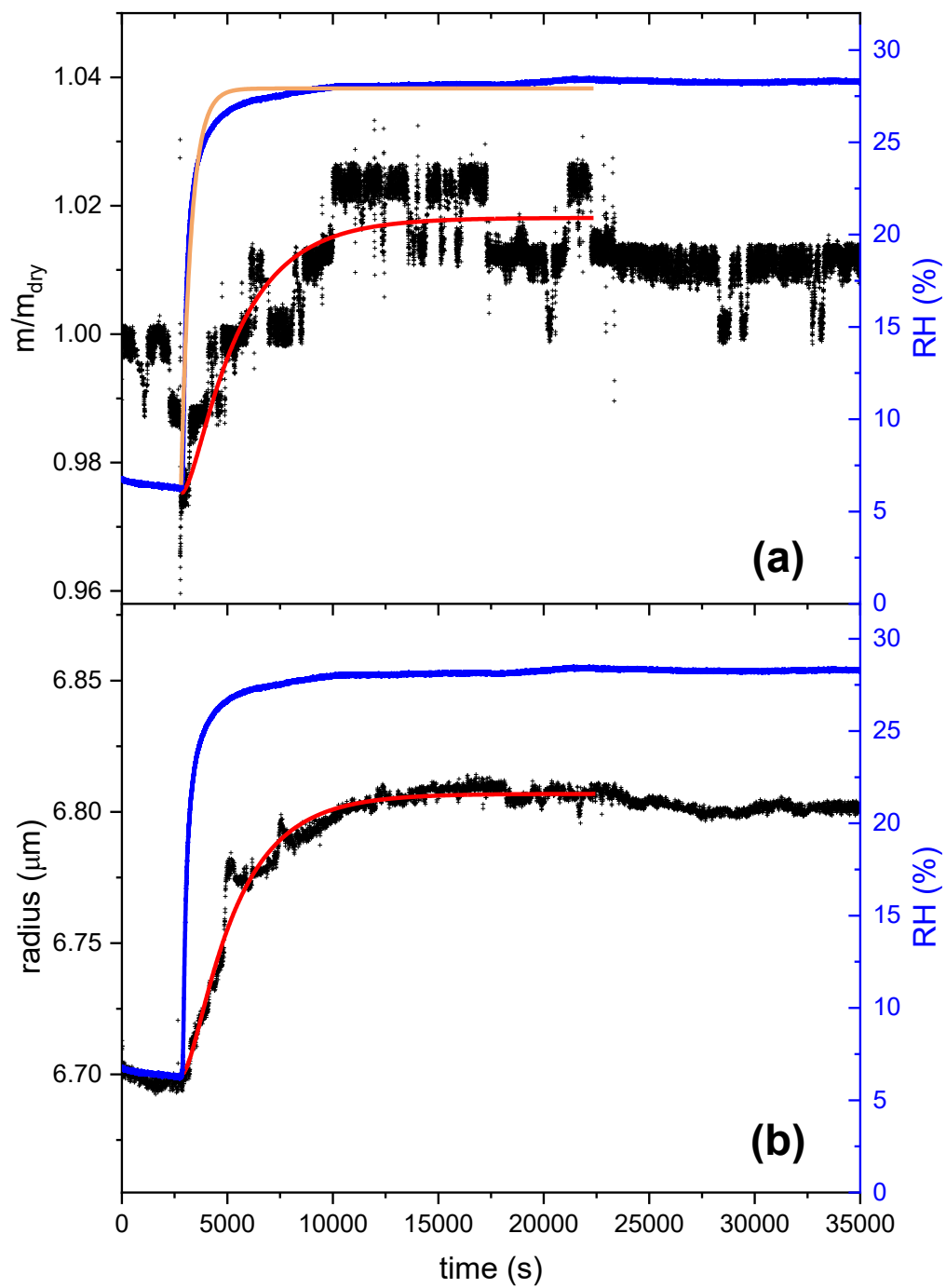
236 Viscosity can then be predicted from diffusivity using Stokes–Einstein relation (Einstein, 1905):

$$237 \quad D = \frac{KT}{6\pi\eta R_{diff}} \quad (6)$$

238 where D is the diffusion coefficient, K is the Boltzmann constant, T is the temperature, η is the viscosity, and R_{diff}
 239 is the radius of the diffusing species. While this relation works well for large diffusing molecules in which the
 240 radius of the diffusing molecule (R_{diff}) is greater than that of the organic matrix molecule (R_{matrix}) (Chenyakin
 241 et al., 2017), it underestimates the diffusion coefficients in organic–water mixtures by several orders of magnitude
 242 for small diffusing molecules like water, where R_{diff} is smaller than R_{matrix} (Price et al., 2015; Bastelberger et
 243 al., 2017). A better approach to relate diffusivity to viscosity is to use fractional Stokes–Einstein relation where D
 244 is proportional to $1/\eta^\xi$, ξ being the fractional exponent, which depends on the ratio R_{diff}/R_{matrix} (Evoy et al.,
 245 2020). For instance, as the ratio R_{diff}/R_{matrix} decreases, ξ decreases (Evoy et al., 2020). ξ can be expressed in
 246 terms of R_{diff}/R_{matrix} according to the following empirical equation (Evoy et al., 2020):

$$247 \quad \xi = 1 - \left[0.73 \exp\left(-1.79 \frac{R_{diff}}{R_{matrix}}\right)\right] \quad (7)$$

248 The hydrodynamic radius of AA (R_{matrix}) was assumed to be the same as that of citric acid, which is structurally
 249 similar to aconitic acid, and was taken as 3.7 \AA (Muller and Stokes, 1957) and for water the Van der Waals radius
 250 of 1.41 \AA (Pang, 2014) was used. The hydrodynamic radius of AA was assumed to remain constant upon aging.



252 **Figure 6: The response of AA to rapid changes in RH after aging with UV and O₃ until 60% mass loss, panel (a) shows**
253 **mass growth data and panel (b) size data. The blue line in both panels shows the RH data (right scale). At time $t = 2,804$**
254 **s, the gas flow was switched from dry to humid with RH increasing rapidly from 6.3% to 28.2% and afterwards kept**
255 **constant for 7.5 h. The black lines represent the response of the aged AA particle in terms of mass (a) and size (b) to the**
256 **rapid increase in RH. The orange line in panel (a) is an exponential fit to the RH data. The red lines are the first-order**
257 **kinetics fitting on the mass response (a) and size (b) response. Fitting was done only up to 22,300 s because after this**
258 **time the mass and size of the particle started to decrease slightly, possibly due to volatilization of some of the remaining**
259 **products or further chemical processing when RH was increased. τ_2 , determined from the RH-fit, was found to be 472**
260 **s. τ_1 , determined from the fitting according to Eq. (4), was found to be 2,503 s for the mass response and 2,312 s for the**
261 **size response. Note: the step-like noise seen in the mass growth data is an artifact of the instrument, mainly due to the**
262 **automatic feedback loop that adjusts the voltage to keep the particle at a fixed position, but with a finite resolution in**
263 **both position and voltage. The dip in mass growth seen just before the RH step is due to sudden changes in the flow**
264 **system when turning on the humid flow after drying.**

265

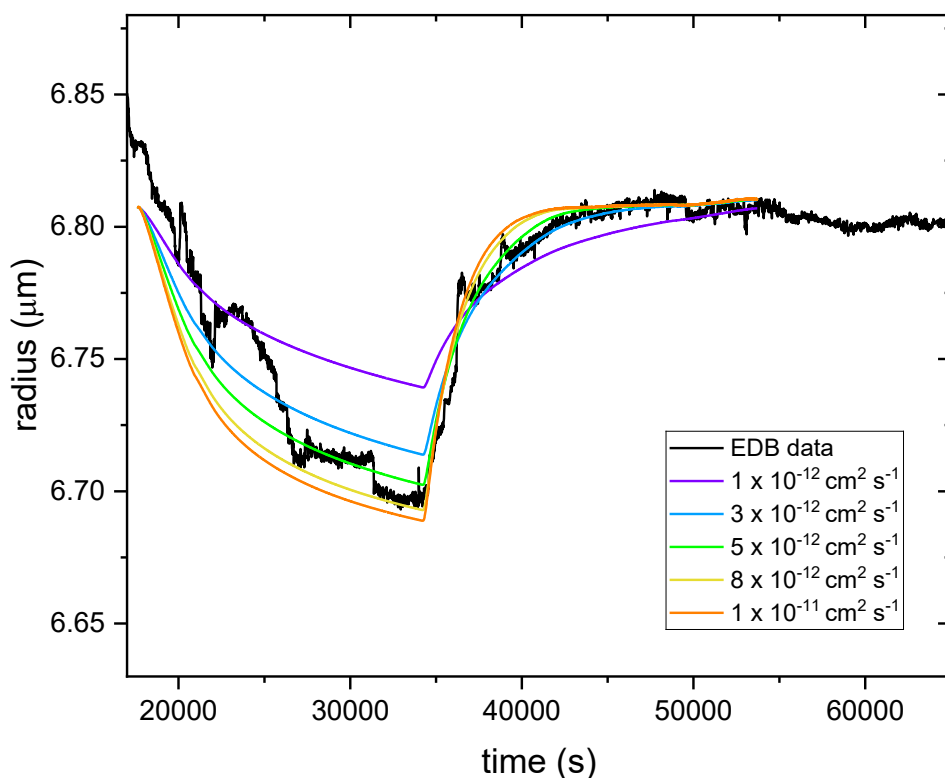
266 **3 Results and Discussion**

267 **3.1 Method validation for the retrieval of diffusivity coefficient of water**

268 To validate our approach of diffusivity coefficient retrieval, D was determined for the same experiment shown in
269 Fig. 6 using the numerical model described in detail in Zobrist et al. (2011). The model treats the particle as
270 consisting of up to several thousand individual shells and uses a composition and temperature dependent
271 parametrization of the diffusion coefficient of water, simulating the growth and shrinkage of the particle resulting
272 from water diffusion between the shells.

273 The model was driven by experimental RH(t) data while drying from 28% to 6% and then humidifying up to 28%
274 as well as the initial radius. For the input, several parametrizations for the water activity dependent diffusivity were
275 tested (see Fig. 7). Parametrization for every input D was derived by linear extrapolation of diffusivity in pure
276 water ($2 \times 10^{-5} \text{ cm}^2 \text{ s}^{-1}$) and input D at $a_w = 0.17$ (ranging from $1 \times 10^{-12} \text{ cm}^2 \text{ s}^{-1}$ to $1 \times 10^{-11} \text{ cm}^2 \text{ s}^{-1}$), assuming that
277 the a_w dependence of D is linear on a log scale.

278 As shown in Fig. 7, considerable agreement between experimental and modelled radius data is obtained when the
279 input D was set between $3 \times 10^{-12} \text{ cm}^2 \text{ s}^{-1}$ and $8 \times 10^{-12} \text{ cm}^2 \text{ s}^{-1}$. D derived for the same particle using the linear
280 response approximation (fitting according to Eq. (4)) is $3 \times 10^{-12} \text{ cm}^2 \text{ s}^{-1}$. In addition, it can be clearly seen that
281 while in the drying part the radius data retrieved from the model for the input $D = 3 \times 10^{-12} \text{ cm}^2 \text{ s}^{-1}$ does not agree
282 well with the experimental data, it agrees quite well after the step increase in RH. This is consistent with D derived
283 from the fitting ($3 \times 10^{-12} \text{ cm}^2 \text{ s}^{-1}$), which is done in the same RH range, i.e. the step increase. Thus, D derived
284 using the two different approaches agree within a factor of 2, which is chosen as the uncertainty range in our
285 determination of D .



286
 287 **Figure 7: Radius data retrieved from the numerical model for different input $D(a_w)$ (colored lines) in the range of $1 \times 10^{-12} \text{ cm}^2 \text{ s}^{-1}$ (violet line) to $1 \times 10^{-11} \text{ cm}^2 \text{ s}^{-1}$ (orange line) for $D(a_w = 0.17)$ in comparison to the experimental radius data**
 288 **(black line) for AA particle subjected to a rapid increase in RH after aging with UV and O_3 until 60% mass loss. Note:**
 289 **in the modeled data, the initial radius at RH 28% (for all input D) is slightly lower than the equilibrium radius at the**
 290 **same RH after the step increase. This is because of the uncertainty in size data, as described in Appendix A.**
 291

292
 293 **3.2 Kinetics: comparison between ozonolysis and photolysis**

294 Figure 8 shows the normalized mass remaining calculated from the voltage data compensating for the gravitational
 295 force as shown in Fig. 4. The mass of an aqueous AA particle remains constant in the absence of UV irradiation at
 296 375 nm or O_3 exposure, indicating that AA has a low vapor pressure and does not undergo any reaction in the
 297 presence of oxygen. In the presence of UV irradiation and/or O_3 exposure, mass loss is observed, which is evidence
 298 for the occurrence of fragmentation reactions that eventually lead to the formation of volatile products that partition
 299 from the particle phase to the gas phase. Fragmentation reactions are known to be an important pathway for organic
 300 aerosol particles undergoing photochemical reactions as well as for particles exposed to oxidants (Dou et al., 2021;
 301 Kroll et al., 2015; Sun and Smith, 2024; O'Brien and Kroll, 2019). However, as shown in Fig. 8, only slight mass
 302 loss is observed when photolysis is done under a nitrogen gas phase, highlighting the importance of oxygen in the
 303 photolysis mechanism. Acceleration in mass loss during photolysis of SOA when transitioning from nitrogen to
 304 zero air was also observed previously in a different study (Sun and Smith, 2024).

305 The decay kinetics of an AA particle upon reaction with ozone is linear with time, similar to a previous study
 306 (Willis and Wilson, 2022), The slow kinetics observed for ozonolysis may be due to the conjugated structure of
 307 AA, which stabilizes the C=C double bond. According to the study by Willis and Wilson (2022), most of the
 308 reactions between O_3 and AA occur in the particle bulk due to the slow reaction of AA with O_3 and AA's low
 309 surface affinity.

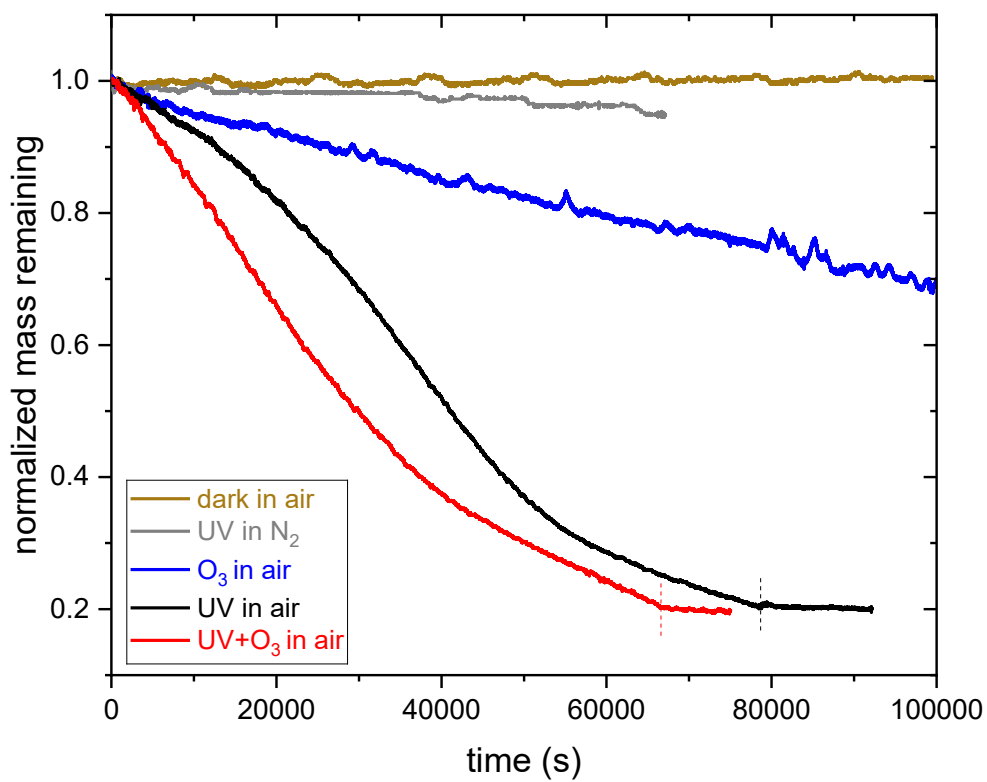
310 In contrast to ozonolysis, the shape of the photolysis decay kinetics is not linear. It is slow in the beginning, then
 311 speeds up possibly due to the formation of more photoreactive intermediates or due to the initiation of an
 312 autocatalytic process. After about 60% mass loss, the reaction slows down again, most likely because most

313 photoreactive species are consumed and non-absorbing products are formed (photobleaching) or because of radical
314 recombination. We conclude that similar to the findings by O'Brien and Kroll (2019) and Sun and Smith (2024),
315 initial photolytic mass loss cannot be extrapolated to the entire SOA mass loss and that a photo-recalcitrant fraction
316 remains, which prevents or slows down further mass loss. In the study by Sun and Smith (2024), Suwanee River
317 Fulvic Acid (SRFA) was used as a surrogate for brown carbon SOA. They observed that UV photolysis of an
318 aqueous SRFA solution results in photobleaching at UV wavelengths and enhanced absorbance
319 (photoenhancement) at visible wavelengths (Sun and Smith, 2024). For AA, UV aging most likely results initially
320 in photoenhancement. As the reaction proceeds, photobleaching occurs due to degradation of chromophores during
321 fragmentation, resulting in a photo-recalcitrant fraction. These findings suggest that even a small precursor
322 molecule, such as AA, might demonstrate a behavior similar to atmospheric brown carbon, exhibiting an alteration
323 of optical properties upon UV aging. However, further investigations are needed to prove that this mechanism is
324 responsible for the observed kinetics.

325 Moreover, it can be inferred from Fig. 8 that the rate of decay of AA is slightly faster when photolysis is done in
326 the presence of O₃. Since ozone is a stronger oxidant compared to oxygen, it might result in a faster mass loss,
327 especially in the beginning of the reaction, where the oxidant is most likely the limiting factor. After the initial
328 induction period, the rates of both reactions become comparable because of the occurrence of acceleration in the
329 absence of O₃.

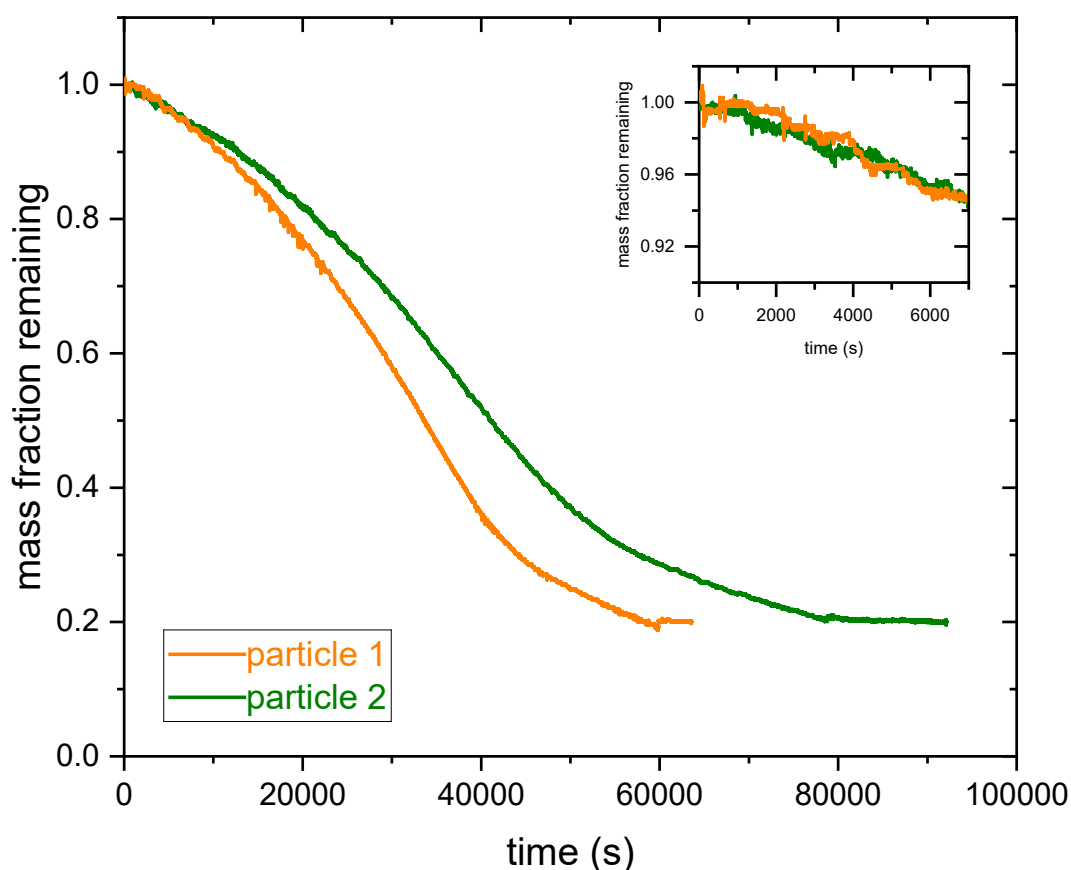
330 Additionally, regarding the photolysis experiments, it can be inferred from Fig. 9 that the rates of reaction of two
331 different AA particles with UV irradiation overlap in the beginning of the experiment, but acceleration in mass loss
332 of particle 1 occurs before particle 2. For instance, after an exposure time of 40,000 s, particle 1 lost 64% of its
333 mass whereas particle 2 lost 48% (see Fig. 9). This is most likely because oxygen is the rate limiting factor in the
334 beginning of the reaction. As the reaction proceeds, the intensity of the UV irradiation becomes important, which
335 results in different reaction rates. This might be due to slightly different particle sizes and the position of the particle
336 relative to the laser beam, which can affect the photon flux into the particle and thus the reaction rate. For this
337 reason, mass loss was used instead of exposure time to represent the extent of aging, as will be presented in the
338 following sections. However, mass loss and exposure time are well correlated (see Fig. E-1 in the appendix), but
339 mass loss was chosen to account for the differences between different particles in terms of the reaction rate,
340 assuming that at a certain mass loss, rather than exposure time, different particles should have similar chemical
341 composition despite having different reaction rates.

342



343

344 **Figure 8: Comparison of the decay kinetics of an AA particle exposed to 375 nm UV irradiation in pure nitrogen and in**
 345 **synthetic air, 10 ppm O₃ in synthetic air, and UV+O₃ in synthetic air. Vertical dashed lines correspond to switching off**
 346 **UV (black) and UV+O₃ (red).**

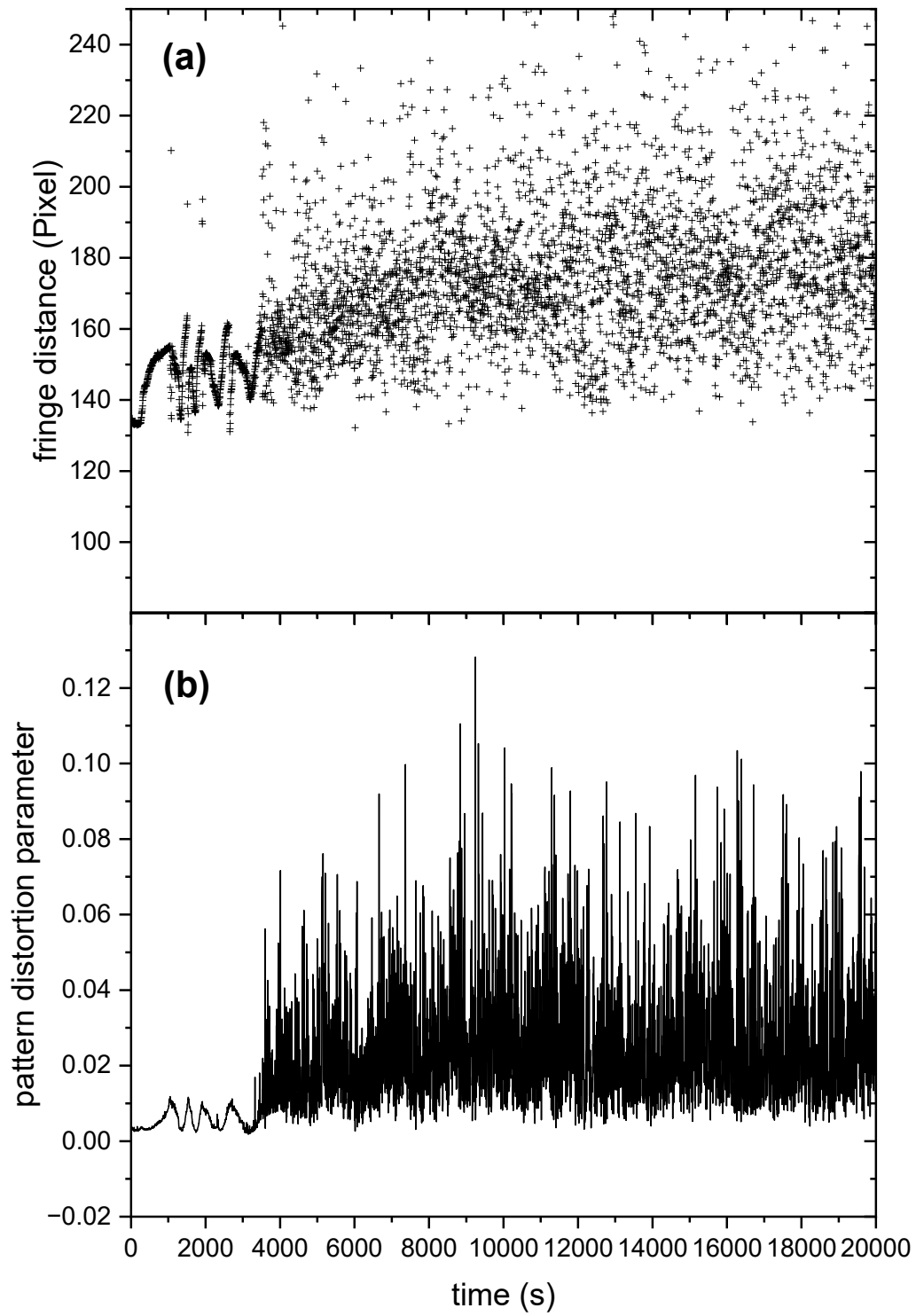


347
 348 **Figure 9: Comparison of the decay kinetics between two different AA particles exposed to 375 nm UV irradiation until**
 349 **80% mass loss. The inset graph shows the first 7,000 s to emphasize the overlap in the initial reaction rate between the**
 350 **two experiments.**

351
 352 **3.3 Phase separation during ozonolysis**

353 Figure 10 shows the mean fringe distance (a) and pattern distortion parameter (b) of a 532 nm laser-illuminated
 354 AA particle upon exposure to ozone. After about an hour of O₃ exposure, the TAOS pattern of the particle becomes
 355 irregular and the pattern distortion parameter, which denotes the asymmetry in the scattering pattern (Braun and
 356 Krieger, 2001), becomes larger. This indicates that the particle is no longer homogenous and spherical and has lost
 357 its symmetry, resulting in light scattering with different intensities depending on its orientation relative to the laser
 358 beam. This behavior was observed only upon exposure to O₃ and was confirmed through five other O₃ exposure
 359 experiments, where an irregularity in the TAOS pattern was observed for all particles after an exposure time of 65
 360 ± 8 min. On the contrary, AA particles exposed to UV illumination or UV and O₃ simultaneously remained
 361 spherical symmetric upon aging (see Fig. F-1 in the appendix). The observed heterogeneity in the particle upon
 362 ozonolysis could be due to liquid-liquid phase separation (LLPS) exhibiting partial wetting morphology. Similar
 363 behavior was observed in other studies upon ozonolysis of oleic acid particles (Hosny et al., 2016) and squalene
 364 droplets (Athanasiadis et al., 2016). However, in the case of ozonolysis of oleic acid, they observed a wide range
 365 of species: small oxidized polar molecules and large non-polar oligomers, which are immiscible and can favor
 366 LLPS. Here, we did not perform chemical characterization of the ozonolysis products, but Willis and Wilson (2022)
 367 identified products having two to seven carbon atoms with different carbon oxidation states (~1 to 3) in AA
 368 ozonolysis experiments. It might be possible that some of the small products with high carbon oxidation state are
 369 immiscible with the larger products with low oxidation state, which can cause phase separation. Another possibility
 370 for the observed symmetry loss in light scattering would be precipitation of *trans*-aconitic acid or one of the
 371 ozonolysis products that is insoluble in water, creating two phases: solid precipitate and dissolved liquid phase,

372 since the particles contain significant amount of water as they are kept at relatively high RH (above 78%), while
373 still being lower than the deliquescence RH of AA, which is $\sim 96\%$ based on our measurements.



375 **Figure 10: (a) Mean fringe distance and (b) pattern distortion parameter of 532 nm laser-illuminated AA exposed to O₃.**
376 **Only the data for the first 20,000 s are plotted here to present clearly the phase transition occurring at ~3,500 s, indicated**
377 **by the significant increase in fluctuations in fringe distance (a) and pattern distortion parameter (b).**

378

379 3.4 Phase state of AA after aging

380 Untreated AA particles typically effloresced at RH ~59.9%, but some particles did not crystallize upon drying to
381 RH below 10%. In contrast, AA particles aged with UV or UV and O₃ simultaneously did not crystallize upon
382 drying. This was deduced from the TAOS pattern, which remained regular upon drying, implying that the aged
383 particles remained liquid or amorphous solid, but not crystalline. After AA particles undergo chemical reaction, a
384 mixture of products is produced, which makes efflorescence less likely to occur due to thermodynamic reasons
385 (Marcolli et al., 2004).

386 Similar behavior in terms of suppression or inhibition of efflorescence after aging was observed previously. For
387 instance, suppression of crystallization was observed upon ozonolysis of mixed maleic acid/ammonium sulfate
388 particles and subsequent drying (Chan and Chan, 2012). In another study, maleic acid particles exposed to O₃
389 showed efflorescence at lower RH compared to unprocessed maleic acid particles, with some particles not
390 efflorescing at any RH (Pope et al., 2010).

391 Furthermore, for AA particles aged with UV or UV and O₃ only up to 20% or 26% mass loss, although the particles
392 remained spherical upon drying, the TAOS pattern became irregular after RH was increased rapidly from 6% to
393 28%, indicating crystallization of AA (see Appendix G). This could be due to restructuring the hydrogen bonding
394 network favoring nucleation. Alternatively, if nucleation already occurred during drying, the plasticizing effect of
395 water could lead to crystal growth after water uptake. This behavior was not observed for particles that lost more
396 than 25% of their mass because of the conversion of considerable amount of *trans*-aconitic acid into a mixture of
397 products, which inhibited crystallization.

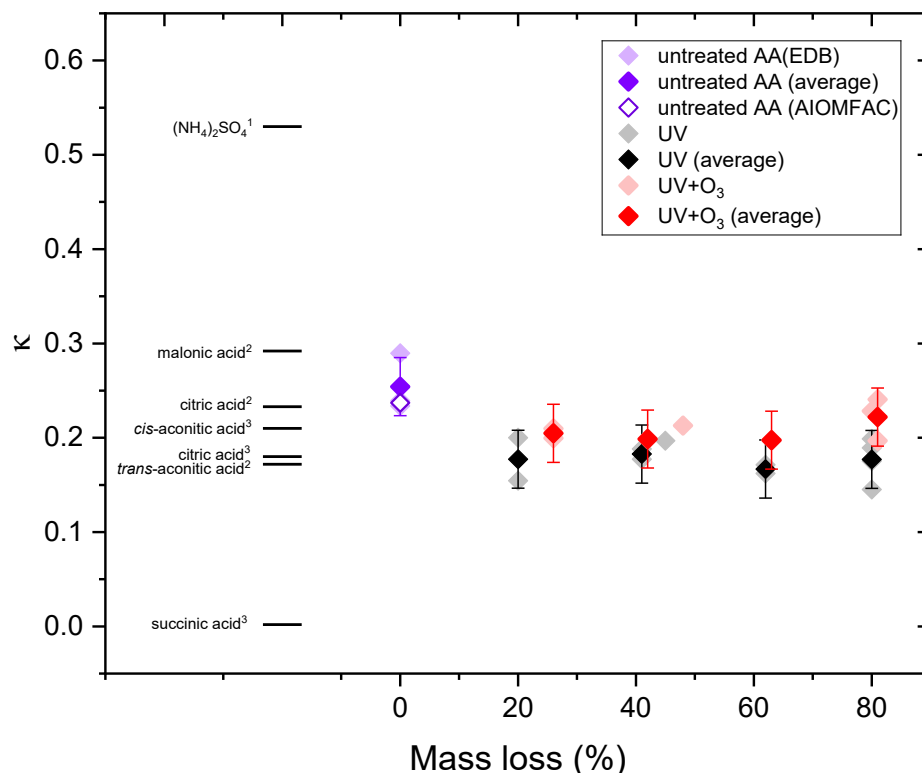
398

399 3.5 Viscosity and hygroscopicity of AA before aging

400 The average viscosity of untreated AA derived from our experiments at room temperature (~298K) and RH $17.7 \pm$
401 0.5% (midpoint of the step in RH 6–28%) is 1.2×10^3 Pa s. Aconitic acid and citric acid are structurally similar:
402 both are tricarboxylic acids having 6 carbon atoms. Song et al. (2016) measured the viscosity of citric acid by
403 droplet coalescence at ambient temperature and reported as 5.1×10^3 Pa s at 18 % RH, which is within a factor of
404 4 of the viscosity of AA determined in this study. The slightly higher viscosity of citric acid compared to aconitic
405 acid might be due to the additional hydroxyl group, which enhances hydrogen bonding (Rothfuss and Petters,
406 2017) and the lower temperature of the coalescence experiment.

407 Figure 11 shows the hygroscopicity results in terms of derived κ values. For reference, a selection of κ values of
408 other organic acids and ammonium sulfate are taken from the literature. As shown in this figure, organic acids can
409 have quite different κ values, but are significantly lower than inorganic salts. Higher κ values indicate higher
410 hygroscopicity (Petters and Kreidenweis, 2007). Hygroscopicity of organic compounds depends on molecular
411 structure and physicochemical properties. Organic compounds having more functional groups, such as carboxyl,
412 carbonyl, and hydroxyl tend to be more hygroscopic (Han et al., 2022). In general, polar organic compounds having
413 higher O:C are more hygroscopic (Han et al., 2022; Lambe et al., 2011; Duplissy et al., 2011). In addition, organic
414 compounds that are more water soluble tend to be more hygroscopic because they would have a higher molar
415 concentration in the saturated solution corresponding to a stronger reduction in water activity (Han et al., 2022).

416 Average κ of untreated AA measured in this study is 0.254 ± 0.031 , which agrees within error with *cis*-aconitic
417 acid (0.21) determined in another study (Han et al., 2022) and that predicted by AIOMFAC model (0.237) (Zuend
418 et al., 2011; Zuend et al., 2008), but is significantly higher than that of *trans*-aconitic acid (0.172 ± 0.010)
419 determined in another study (Rickards et al., 2013). In our study, fitting was done between RH 62% and 80%,
420 which is different from the RH used in Rickards et. al (> 90%), which could be one reason for the difference.
421 Variations in κ for the same organic acid between different studies have been observed previously. For instance, as
422 shown in Fig. 11, κ for citric acid determined using a humidified tandem differential mobility analyzer (HTDMA)
423 at RH 90% was found to be 0.18 (Han et al., 2022), while that determined using aerosol optical tweezers (AOT)
424 at RH 66% was found to be 0.233 ± 0.035 (Rickards et al., 2013). In the following, we focus on changes in κ with
425 aging rather than on absolute κ values.



427

428 **Figure 11: The hygroscopicity of AA particles before and after UV and UV+O₃ aging in comparison with (NH₄)₂SO₄,**
 429 **malonic acid, citric acid, cis-aconitic acid, trans-aconitic acid, and succinic acid data taken from the literature: (1)**
 430 **(Petters and Kreidenweis, 2007) (2) (Rickards et al., 2013) (3) (Han et al., 2022).**

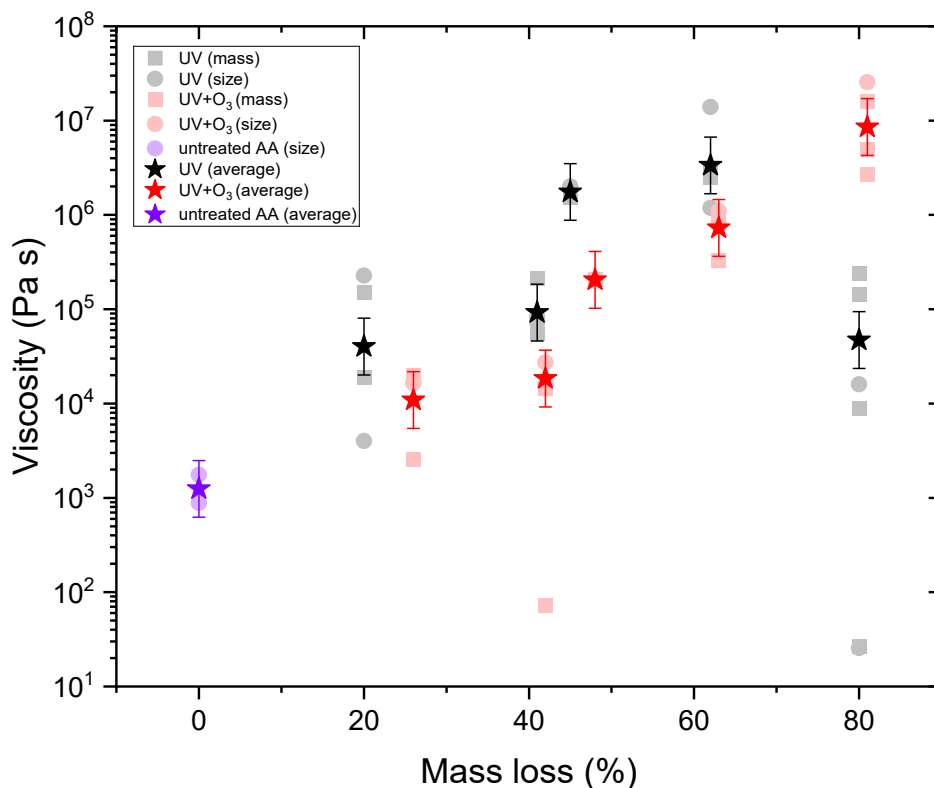
431

432 3.6 Viscosity and hygroscopicity of AA after aging

433 Figure 12 shows the viscosity of untreated AA and AA aged with UV and UV and O₃ simultaneously up to 20%,
 434 40%, 50%, 60%, and 80% mass loss. All measurements were done at room temperature (~298 K) and at RH 17.7
 435 ± 0.5%. It should be noted that the viscosity estimates represented here are lower limit estimates. This is because
 436 we are assuming a constant fractional exponent (ξ) even though the composition of the matrix is changing
 437 significantly upon aging. Since smaller fragmentation products volatilize and are lost to the gas phase, R_{matrix}
 438 is expected to increase upon aging, thus the ratio R_{diff}/R_{matrix} is expected to decrease. This leads to larger viscosity
 439 values when estimating from water diffusivity data using fractional Stokes–Einstein.

440 As shown in Fig. 12, the viscosity of AA exposed to UV and O₃ simultaneously increased with the extent of aging,
 441 with the aged AA at 80% mass loss being almost 4 orders of magnitude higher compared to that of the untreated
 442 AA. UV exposure alone also resulted in an increase in viscosity but only up to 60% mass loss. Surprisingly, further
 443 UV-aging (80% mass loss) led to a reduction in viscosity. However, with UV-aging at 80% mass loss, there is a
 444 large spread in the viscosity data, where some of the values at the lower viscosity range were beyond the limit of
 445 determination with our method (see Appendix D). Since the discrepancies in the viscosity values are mainly
 446 between size and mass measurement for the same particle, rather than being between different experiments, the
 447 uncertainty is most likely due to experimental error at 80% mass loss, where the particle becomes small, increasing

448 the error on both size and mass measurements. Thus, it is difficult to conclude the exact viscosity at 80% mass
449 loss, but it is evident that the viscosity in all cases is significantly less than the one at 60% mass loss.



450
451 **Figure 12: The viscosity of AA particles before and after UV and UV+O₃ aging from mass and/or size data.**

452
453 As shown in Fig. 11, average κ of aqueous AA particles decreased slightly from 0.254 ± 0.031 to 0.177 ± 0.031
454 upon aging with UV light till 20% mass loss. Upon further aging, κ remained almost constant. For the AA particles
455 aged with UV and O₃ simultaneously, less significant reduction in κ was observed. Similar to UV-aging, κ
456 decreased from 0.254 ± 0.031 to 0.205 ± 0.031 after 25% mass loss, but then it remained almost constant with
457 further aging. However, this reduction is not significant, taking the uncertainty in κ into account. In addition,
458 overall κ values for UV+O₃ aged AA are a bit higher than those of UV-aged AA, consistent with the viscosity
459 values, which show slightly lower viscosity for UV+O₃ aged AA up to 60% mass loss.

460 Currently, we do not have any information about the chemical composition of the particles after aging. However,
461 we may draw some conclusions from the data shown in Fig. 11 and 12. Since hygroscopicity did not increase after
462 aging, O:C is also expected to remain almost constant or decrease slightly after aging. While it is known that
463 hygroscopicity and carbon oxidation state increase after oxidative aging (Jimenez et al., 2009; Kroll et al., 2011;
464 Kroll et al., 2015), no significant or small net change in O:C was observed after photolysis of SOA in other studies
465 (Romonosky et al., 2015; O'Brien and Kroll, 2019). It should be noted that in this study, only the hygroscopicity
466 and viscosity of the condensed phase after aging are measured, without considering the highly volatile compounds
467 evaporating to the gas phase. It is still expected that the overall carbon oxidation state increased after aging in our
468 study if the compounds lost to the gas phase are also considered. As gas phase oxidants are involved in the aging
469 process (O₂ in UV-aging and O₃ in UV+O₃ aging), it is expected that polar oxygen containing functional groups
470 are added after oxidation. Since these groups weaken adjacent C-C bonds, fragmentation reactions will take place,
471 leading to volatilization of smaller fragments to the gas phase. This mechanism can be indirectly inferred from Fig.
472 8, where initially an induction period appears, followed by rapid mass loss. However, it is expected that the most
473 highly oxidized carbon will exist mainly in the gas phase (Kroll et al., 2011). Therefore, although the small,
474 fragmented products are expected to have higher oxidation state, they are also expected to be volatile, thus the

475 oxidation state of the particle can decrease slightly after these fragments evaporate (O'Brien and Kroll, 2019;
476 Hildebrandt Ruiz et al., 2015). However, we cannot prove that O:C remained constant or decreased slightly, since
477 we did not determine the chemical composition of the products. Note that if O:C increased after aging, but if the
478 average molecular weight increased as well, the hygroscopicity may still decrease.

479 Viscosity increase upon SOA aging was observed previously in the UV-aging of d-limonene and α -pinene SOA
480 (Baboomian et al., 2022). Mass spectrometric analysis indicated that the increase in d-limonene SOA viscosity was
481 most likely due to changes in the chemical properties because an average increase in molecular weight, elemental
482 O:C ratio, number of carbon atoms per molecule, and double bond equivalent was observed (Baboomian et al.,
483 2022). However, in contrast to our study, photolysis of SOA was done at low RH. Water content of the particle
484 during photolysis can play an important role in the mechanism of formation of products and thus in the viscosity
485 of the final products. For instance, when photolysis of SOA was performed in aqueous solution instead of low RH,
486 reduction in carbon number was observed, which was attributed to the degradation of dimers and trimers
487 (Romonosky et al., 2015). Another study comparing condensed-phase SOA photolysis at low RH and aqueous
488 photolysis found that the signal intensity obtained by mass spectrometry in the larger m/z range remained similar
489 before and after exposure, while lower m/z range was higher after aqueous photolysis, but lower after condensed-
490 phase photolysis (Sun and Smith, 2024). They attributed this difference to the evaporation of the volatile products
491 from the condensed phase, but retention of these species in the aqueous solution. Direct comparison of our study
492 to these studies is difficult, since in our case condensed-phase photolysis was done at higher RH. However, since
493 mass loss was observed and the viscosity increased after UV-aging, it can be inferred that the smaller volatile
494 fragments evaporated, leaving relatively larger non-volatile products in the particle.

495 One possible explanation for the observed viscosity enhancement after aging is the formation of oligomers from
496 product fragments. Oligomers, due to their high molecular weight, could contribute to increased viscosity.
497 However, the formation of oligomers might be hindered under the experimental conditions, as the reactions occur
498 at moderately high RH, and the presence of water typically slows down oligomerization (Kalberer et al., 2004). It
499 is important to note, though, that the particles are more concentrated in water at these RH levels (even at 85%)
500 compared to typical aqueous-phase chemistry, which may facilitate oligomer formation. Additionally,
501 oligomerization could have occurred during the drying process just before viscosity measurements were taken.

502 Alternatively, the increase in viscosity could be attributed to changes in the hydrogen bonding network. The
503 intermolecular hydrogen bonding between the products might be enhanced compared to untreated AA, leading to
504 a higher viscosity. Further UV-aging could degrade some of these products or the oligomers, potentially altering
505 the hydrogen bonding interactions and causing a decrease in viscosity upon continued aging.

506 The continuous increase in viscosity upon aging with UV and O₃ simultaneously until 80% mass loss suggests that
507 the aging mechanism and the products formed are different in the presence of oxidants like O₃. The presence of O₃
508 might favor the formation of oligomers, therefore increasing the viscosity of the particles further with longer
509 exposure.

510

511 **4 Conclusion**

512 In this study, the viscosity and hygroscopicity of aqueous *trans* aconitic acid particles were determined after
513 exposure to 375 nm UV irradiation or UV irradiation and O₃. Photolysis and ozonolysis resulted in significant
514 mass loss because of fragmentation reactions followed by volatilization and displayed different reaction kinetics.
515 Ozonolysis alone disrupted the light scattering symmetry of the particle, indicating a phase transition. Aging with
516 UV or UV and O₃ resulted in the inhibition of efflorescence upon drying. The viscosity of the particles increased
517 by almost 4 orders of magnitude upon aging with UV and O₃ simultaneously. UV-aging also resulted in an increase
518 in viscosity but only up to 60% mass loss. Further UV-aging resulted in a reduction in viscosity. Hygroscopicity
519 of the particles decreased slightly after exposure to UV laser up to 20% mass loss and then stayed constant with
520 further aging. A similar trend, though less significant, was observed for combined UV and O₃ aging.

521 To check the relevance of our study to atmospheric conditions, we estimated the characteristic mixing times within
522 the particles after aging. The increase in viscosity upon aging implies for particles with a radius of 100 nm (typical
523 of accumulation mode SOA particles) a characteristic mixing time of 4 h compared to 4 s for the unexposed
524 particles under dry boundary layer conditions, at RH ~ 17% and 298 K. For colder temperatures in the free
525 troposphere, the mixing times could be still longer even at higher relative humidity. As a result, higher viscosity

526 and mixing times are expected to extend particle lifetime and promote longer-range transport by reducing
527 susceptibility to washout and further chemical processing.

528 Therefore, the changes in viscosity, hygroscopicity, phase state, volatility, and mixing times observed in this study
529 provide further evidence on how aging can directly alter the physicochemical properties of aerosol particles, with
530 indirect consequences on climate and human health. Our results show that the presence of gas phase oxidants like
531 ozone, in addition to UV light, results in viscosity enhancement, an effect seen previously in the UV-aging of SOA.
532 This viscosity enhancement is most likely due to the formation of oligomers of high molecular weight. However,
533 from the shape of reaction kinetics, hygroscopicity, and viscosity results, we conclude that the mechanism of aging
534 is different in the presence of gas phase oxidants compared to photochemical aging without gas phase oxidants.
535 Thus, further studies on simultaneous aging are needed to determine whether the effects observed in this study can
536 be extended to other systems. To understand better the mechanism behind the differences that we observe, we plan
537 to study in the future the chemical composition of the products during aging using mass spectrometry.

538

539

540

541

542

543

544

545

546

547

548

549

550

551

552

553

554

555

556

557

558

559

560

561

562

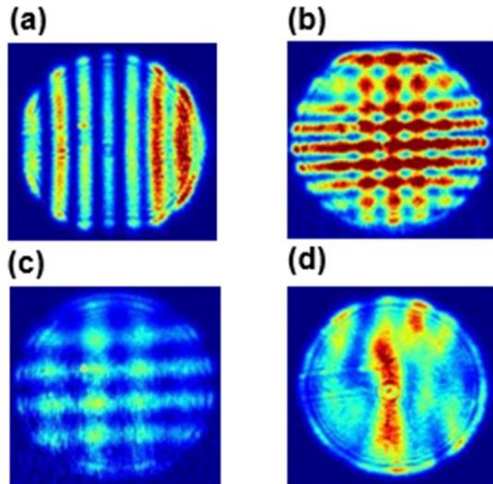
563

564

565
566
567

568 **Appendix A. Size retrieval from two-dimensional angular optical scattering (TAOS) pattern**

569 The EDB configuration and geometrical constraints allow us to measure the TAOS pattern within about 5° half
570 apex angle around 100° scattering. Figure A-1 shows four TAOS-patterns observed in our experiments.

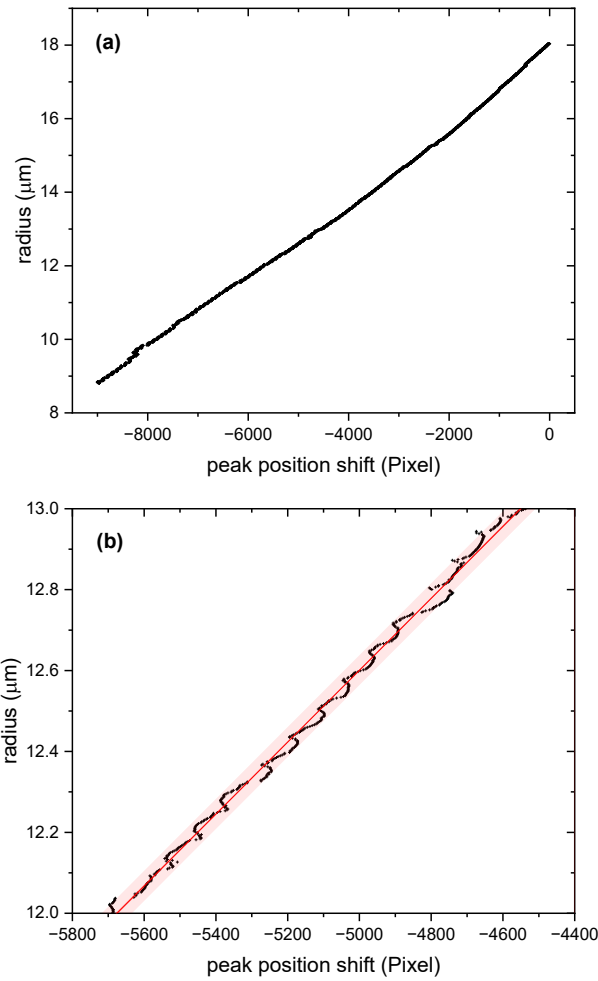


571

572 **Figure A-1: (a) TAOS pattern of a spherical symmetric *trans*-aconitic acid particle upon illumination with polarized 532**
573 **nm laser, fringe intensity is rainbow color coded in arbitrary units. (b) pattern of a particle upon illumination by both**
574 **the polarized 532 nm laser and the orthogonally polarized 375 nm laser. (c) same as (b) but after photochemical aging.**
575 **(d) TAOS pattern for 532 nm illumination only after phase transition induced by ozonolysis.**

576 Comparing Fig. A-1(d) with the other panels of Fig. A-1 illustrate that the regular TAOS pattern is distorted once
577 the spherical symmetry of a particle is lost. In comparison to Fig. A-1(b), the average fringe distance for both
578 orthogonal fringe patterns in Fig. A-1(c) has increased, indicating shrinkage during aging. Quantitative analysis of
579 these types of patterns, i.e. size retrieval, has been discussed extensively in the literature (Davis and Periasamy,
580 1985; Steiner et al., 1999; Jakubczyk et al., 2013; Davies, 2019). A fast, simple method for sizing a spherical
581 symmetric particle is based on scattered light angular frequency determination (Steiner et al., 1999), which requires
582 a calibration of the TAOS pattern in terms of scattering angle. We follow the suggestion by Davies (2019) and
583 measure the evaporation rate of a pure compound for calibration, here PEG-4 for which the vapor pressure is well
584 established (Krieger et al., 2018).

585 Sizing by measuring the characteristic angular frequency works best for scattering angles smaller than 60° .
586 However, our scattering angle is 100° and our apex angle is quite small due to spatial restriction in our setup. This
587 limits its applicability to small size changes, as the uncertainty in sizing using the characteristic angular frequency
588 is of the order of $\pm 1 \mu\text{m}$ for our scattering geometry and typical particle size. Therefore, for measuring small size
589 changes, we apply a method based on spectral shift of Mie-resonance spectra (Zardini et al., 2006) to angular shift
590 of a peak position in the TAOS pattern. Compare this approach with a related method based on tabulated peak
591 positions suggested by Davies (2019). Figure A-2 shows data taken for an evaporating PEG-4 particle at constant
592 temperature. Panel (a) shows that the radius scales almost linearly over a wide size range with the total peak
593 position shift in the TAOS pattern. On closer inspection (see panel (b) of Fig. A-2), the relationship is irregular on
594 small scales but allows the reliable detection of size changes of about $\pm 40 \text{ nm}$. In our application, we are focusing
595 on characteristic time scales of small size changes due to rapid changes in relative humidity: there, the irregularity
596 between size and peak position shift for small size changes influences the determination of characteristic time only
597 slightly (see Fig. 6 in main text.)



598

599 **Figure A-2:** (a) Size data of an evaporation experiment (PEG-4 at 24°C) versus peak position shift. Evaporation rate
600 was calculated from known data of vapor pressure (Krieger et al., 2018) and radius was determined through comparison
601 of measured characteristic angular frequency with evaporation rate. (b) Zoom into the data of (a) showing that radius
602 can be measured with a sensitivity of about ± 40 nm when measuring the peak position shift. Note however, that the
603 relationship between peak position shift and size is not strictly linear, but irregular within a size change of approximately
604 40 nm.

605

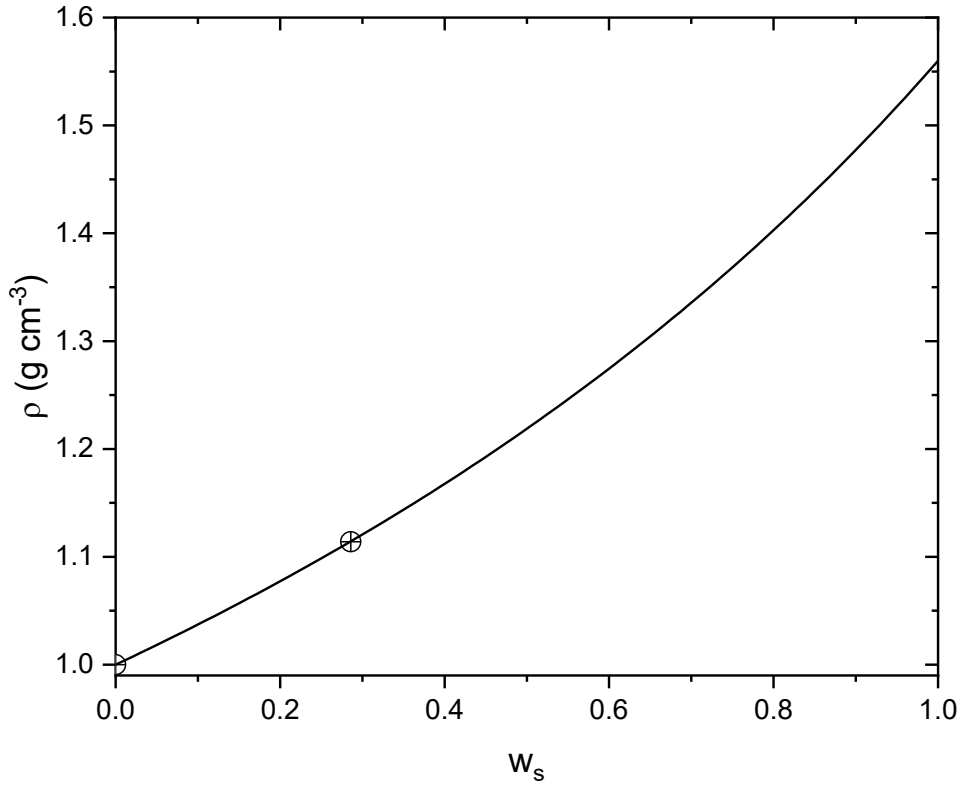
606 **Appendix B.** Density determination of aqueous AA

607 To determine the density of aqueous AA under dry conditions (ρ_0), the density of AA at mass fraction $w_s = 0.286$
608 was measured using a pycnometer. Assuming the conventional additivity rule holds (Lienhard et al., 2012; Steimer
609 et al., 2015):

$$610 \quad \rho(w_s) = \left(\frac{1-w_s}{\rho_w} + \frac{w_s}{\rho_0} \right) \quad (B1)$$

611 where $\rho(w_s)$ is the density of solute at mass fraction w_s , ρ_w is the density of water, we retrieve ρ_0 , the density of
612 aqueous AA solute at dry conditions, i.e. the subcooled melt density. Based on the known density of water and our
613 measured density at $w_s = 0.286$, $\rho_0 = 1.56 \text{ g cm}^{-3}$.

614



615

616 **Figure B-1: Density (ρ) vs. mass fraction (w_s) parametrization for aqueous AA according to Eq. (B1).**

617

618 **Appendix C. Deconvolution of linear response to an exponential ‘step’ in relative humidity, derivation of Eq. (4)**

619 Let’s assume the dynamic system is a linear time-invariant one, with the response of the system to a step input
 620 (Heaviside function, $H(t)$) is given by:

$$621 \quad y(t) = 1 - e^{-k_1 t}$$

622 Now, instead of a step input, $H(t)$, the input function is given by:

$$623 \quad RH(t) = 1 - e^{-k_2 t}$$

624 In our experiment, we obtain k_2 by analyzing the data $RH(t)$, with k_2 being the rate constant of the RH-step. We
 625 want to determine the system’s response $y(t)$ to the input $RH(t)$. Very generally, the system’s response is given
 626 by the convolution integral:

$$627 \quad y(t) = \int_0^t RH(\tau)h(t - \tau) d\tau$$

628 where the impulse response $h(t)$ is the derivative of the system to a step response $H(t)$:

$$629 \quad h(t) = k_1 e^{-k_1 t}, \quad t > 0$$

630 For the step response, $H(t)$, the radius or mass evolution is related to the impulse response by:

$$631 \quad y(t) = \int_0^t h(\tau) d\tau$$

632 Therefore, substituting the RH input function and the impulse response function by

633 $h(t - \tau) = k_1 e^{-k_1(t-\tau)}$, we get:

634
$$y(t) = \int_0^t (1 - e^{-k_2(\tau)}) k_1 e^{-k_1(t-\tau)} d\tau$$

635 Expanding the integral:

636
$$y(t) = k_1 e^{-k_1 t} \int_0^t (1 - e^{-k_2 \tau}) e^{k_1 \tau} d\tau$$

637 Solving the integral leads to the final expression for $y(t)$:

638
$$y(t) = (1 - e^{-k_1 t}) - \frac{k_1}{k_1 - k_2} (e^{-k_2 t} - e^{-k_1 t})$$

639 Replacing the rate constants with their inverse, i.e. the characteristic time constants $\tau_1 = 1/k_1$ and $\tau_2 = 1/k_2$,
640 yields Eq. (4):

641
$$y(t) = (1 - e^{-t/\tau_1}) - \frac{\tau_2}{\tau_2 - \tau_1} (e^{-t/\tau_2} - e^{-t/\tau_1})$$

642

643 **Appendix D.** Comparing the linear response approximation of Appendix C to a numerical model solving the
644 diffusion equation

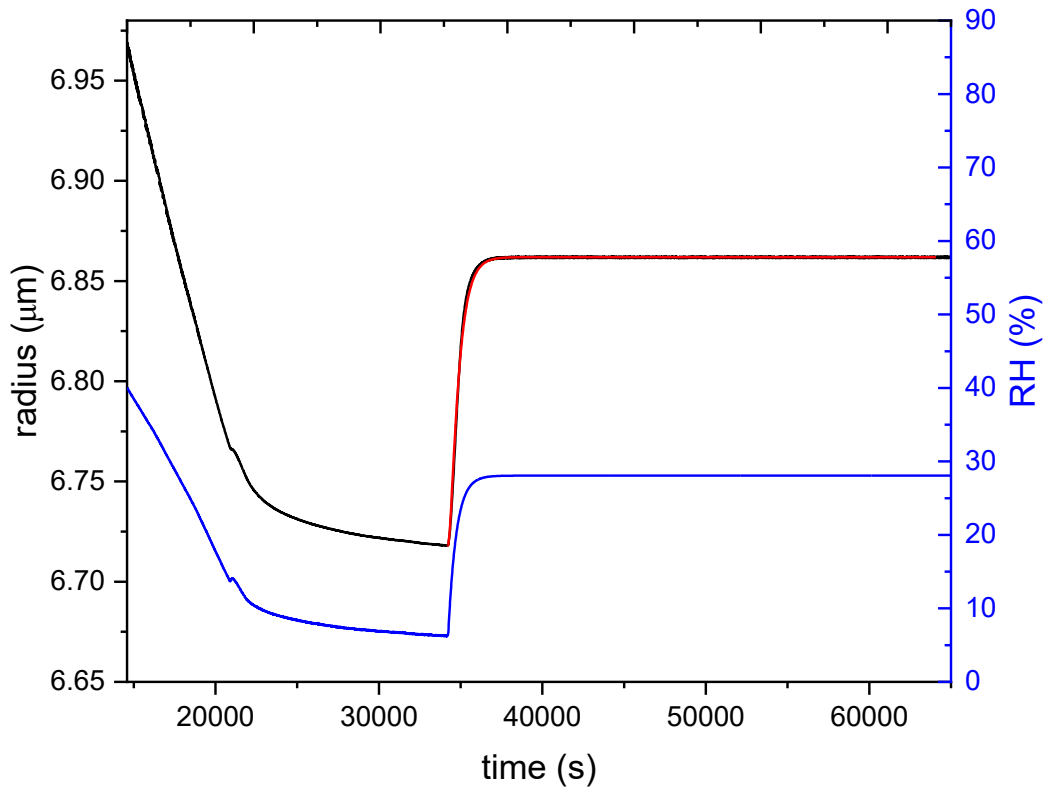
645 As noted in the main text, the linear response approximation for water uptake kinetics is expected to diverge from
646 the full solution of Fick's second law when water diffusivity becomes sufficiently slow. Here, we compare the size
647 change resulting from water uptake under an ideal exponential 'step'-like change in RH, using a numerical model
648 based on the Euler forward method to solve the diffusion equation (Zobrist et al., 2011), with the linear
649 approximation described in Appendix C.

650 Since we use the same flow changes in all our experiments and the particle sizes in the experiments vary only over
651 a rather small size range, we can restrict the comparison to an idealized $RH(t)$ pathway taken from our
652 experimental observations as well as choosing a particular initial radius. Figure D-1 shows the $RH(t)$ pathway
653 chosen as a blue line, the size response predicted by the numerical model as a black line and a linear regression of
654 Eq. (4) to the size predicted by the numerical model as a red line. For simplicity, we assume as input for the
655 numerical model that the dependence of water diffusivity on water activity follows an exponential dependence for
656 water activities with the water diffusivity for pure water fixed to $2 \times 10^{-5} \text{ cm}^2 \text{ s}^{-1}$. At 40% RH, an initial radius of
657 $6.969 \mu\text{m}$ is set and it is assumed that at this starting RH before drying the particle is internally mixed in water
658 content. For the simulation of Fig. D-1, we set the water diffusivity D ($a_w = 0.17$) to $2 \times 10^{-10} \text{ cm}^2 \text{ s}^{-1}$. As evident
659 from Fig. D-1 for these parameters, the linear approximation seems to mirror the predictions of the numerical
660 model very well.

661 Following this approach, we test the linear response for the range of D ($a_w = 0.17$) between $5 \times 10^{-13} \text{ cm}^2 \text{ s}^{-1}$ to $2 \times$
662 $10^{-7} \text{ cm}^2 \text{ s}^{-1}$. Some of the results are shown in Fig. D-2. It becomes clear that our experiments are not sensitive to
663 D (at $a_w = 0.17$) $> 2 \times 10^{-9} \text{ cm}^2 \text{ s}^{-1}$, simply because our experimental setup yields a rather slow response in $RH(t)$
664 upon a step change in gas mass flows (We cannot increase the total flow much beyond 50 sccm to allow mass
665 measurements). For this reason, the second step increase in RH (from 28% to 49%), shown in Fig. 4 in the main
666 text, was not evaluated. Figure D-2 shows in addition the expected deviation from linear response with low water
667 diffusivities (panels e and f).

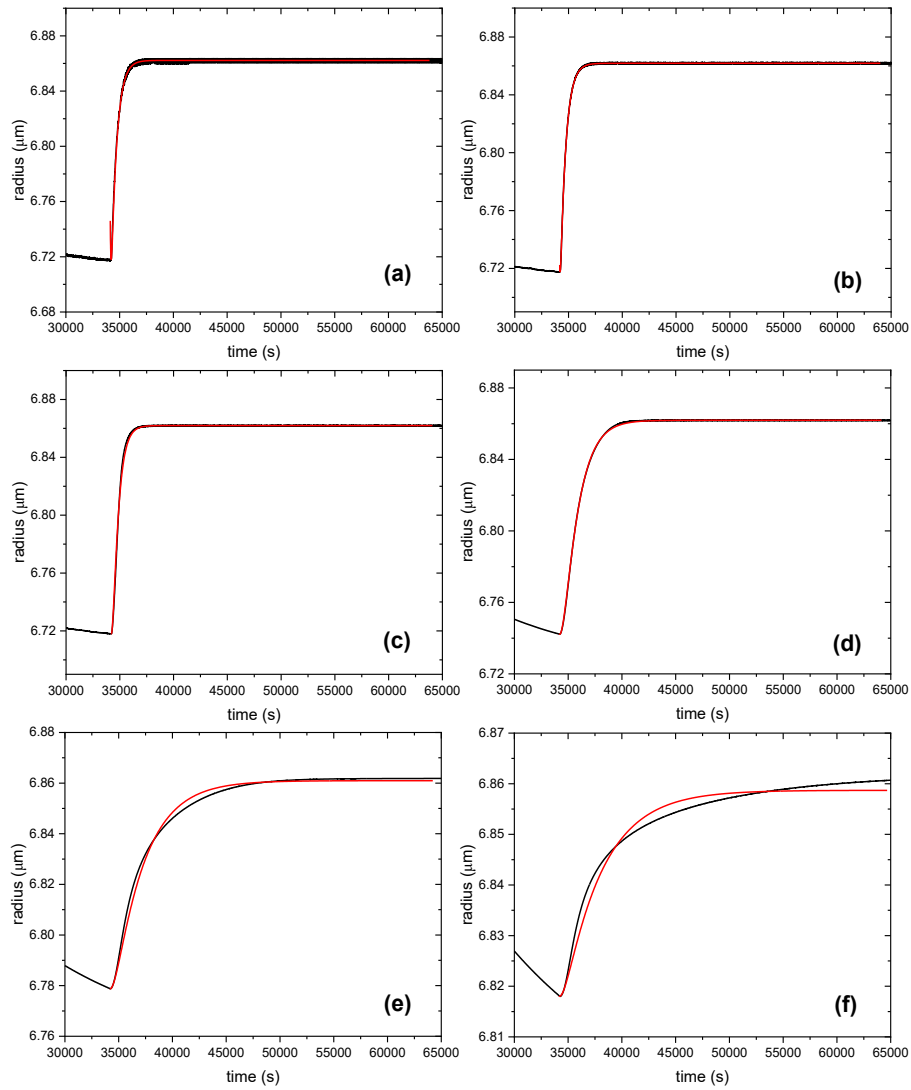
668 However, we can correct for the differences between numerical model and linear approximation for a limited range
669 of water diffusivities as shown in Fig. D-3. There, we compare the characteristic time constant, τ_1 , obtained from
670 the linear regression to Eq. (4) to the input parameters of the numerical model represented as characteristic time
671 according to Eq. (5). Perfect agreement between both is indicated as the dashed line. The limited range of
672 characteristic response times for which the linear approximation works is clearly visible from Fig. D-3. It allows
673 us to deduce an empirical correction factor which we apply for characteristic response times measured in our
674 experiments ranging from 20 s to about 27,000 s. Fortunately, this is approximately the time range we do observe
675 in our experiments for untreated AA and the most viscous aged particles.

676



677

678 **Figure D-1: The blue line represents the RH data. The black line represents the radius data obtained from the numerical**
679 **model for an input D of $2 \times 10^{-10} \text{ cm}^2 \text{ s}^{-1}$. The red line is the first-order kinetics fitting according to Eq. (4) on the size**
680 **response data after increasing RH rapidly.**

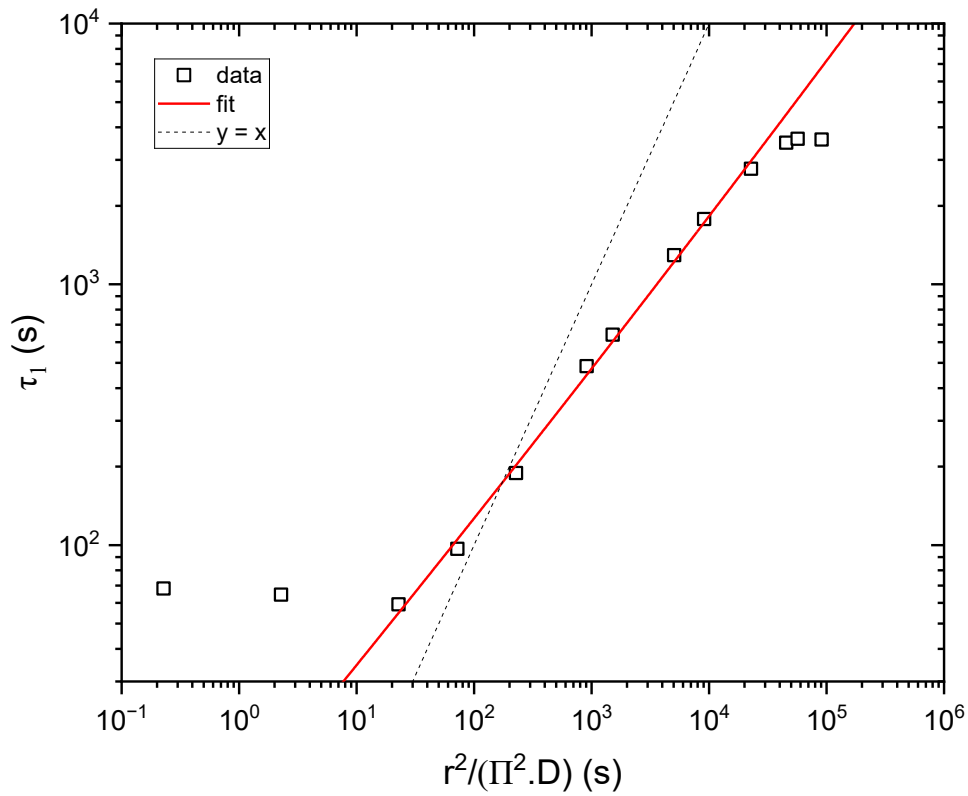


681

682 **Figure D-2: The black line represents the size data obtained from the numerical model for an input D (at $a_w = 0.17$) of**
 683 **(a) $2 \times 10^{-8} \text{ cm}^2 \text{ s}^{-1}$, (b) $2 \times 10^{-9} \text{ cm}^2 \text{ s}^{-1}$, (c) $2 \times 10^{-10} \text{ cm}^2 \text{ s}^{-1}$, (d) $9 \times 10^{-12} \text{ cm}^2 \text{ s}^{-1}$, (e) $2 \times 10^{-12} \text{ cm}^2 \text{ s}^{-1}$, and (f) $5 \times 10^{-13} \text{ cm}^2 \text{ s}^{-1}$.**
 684 **The red line shows the linear response approximation regression curve.**

685

686



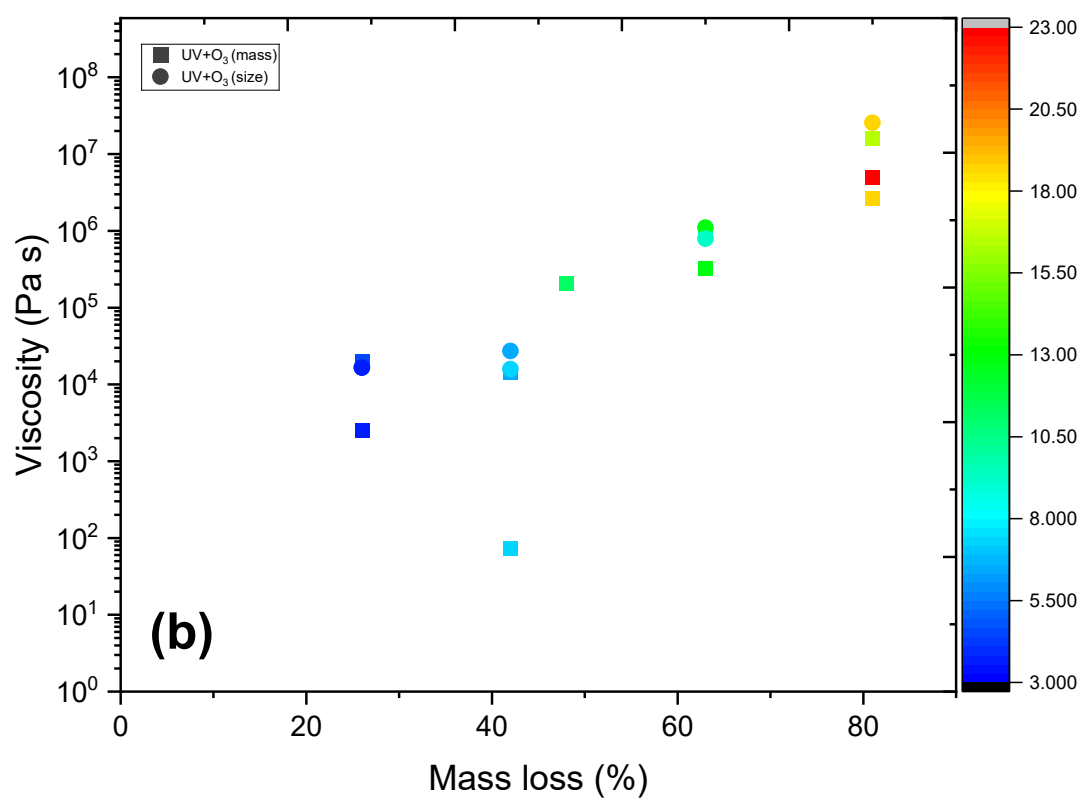
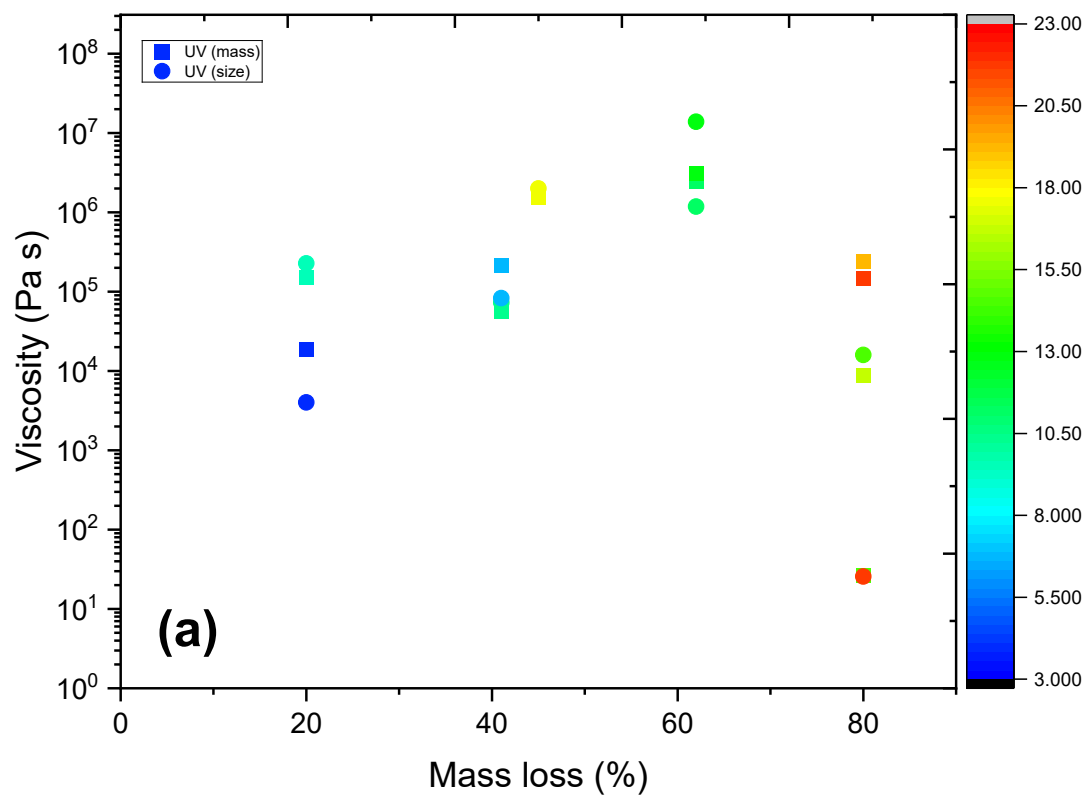
687

688 **Figure D-3: Output τ_1 data determined using the exponential function vs. input $r^2/(\Pi^2.D)$ data determined using the**
 689 **numerical model. The red line represents the fit on the output vs. input data. The dashed line shows $\tau_1 = \frac{r^2}{\Pi^2.D}$.**

690

691 **Appendix E. Correlation between mass loss and exposure time**

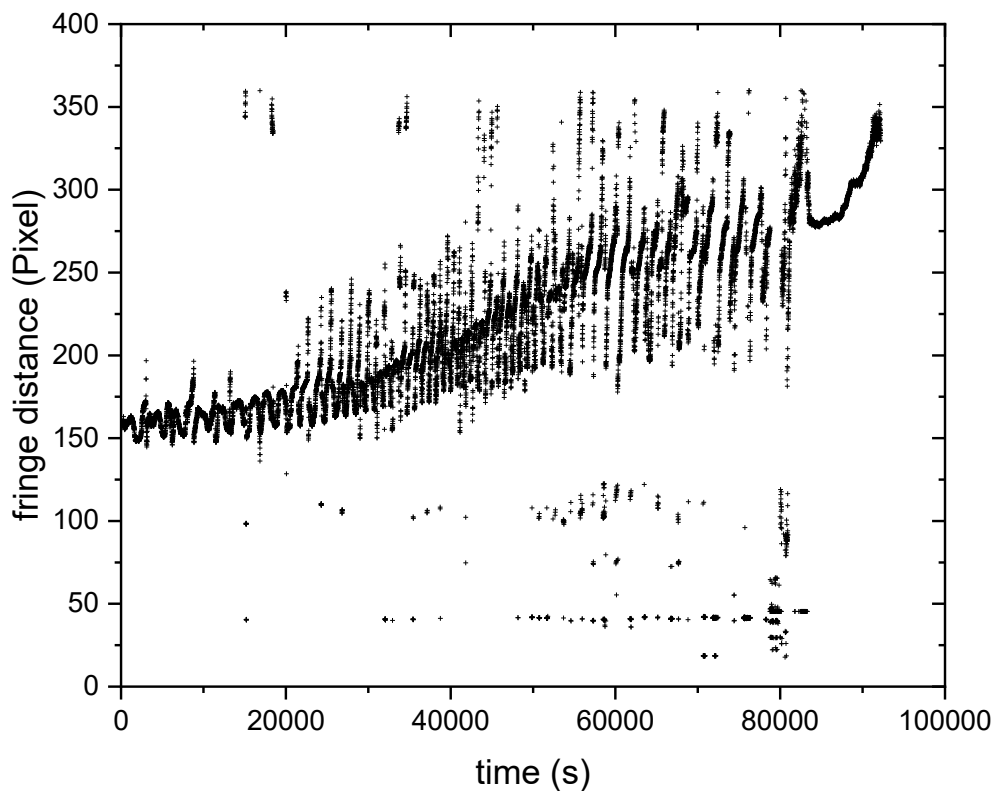
692 Figure E-1 shows that as mass loss increases, exposure time also increases for both UV and UV+O₃ exposure. This
 693 means that mass loss and exposure time are well correlated. Thus, % mass loss can be used to represent the extent
 694 of aging.



696 **Figure E-1: Viscosity of AA particles as a function of mass loss color-coded according to the exposure time (h) for (a)**
697 **UV-exposure experiments and (b) UV+O₃.**

698

699 Appendix F. Mean fringe distance of AA particle exposed to UV up to 80% mass loss

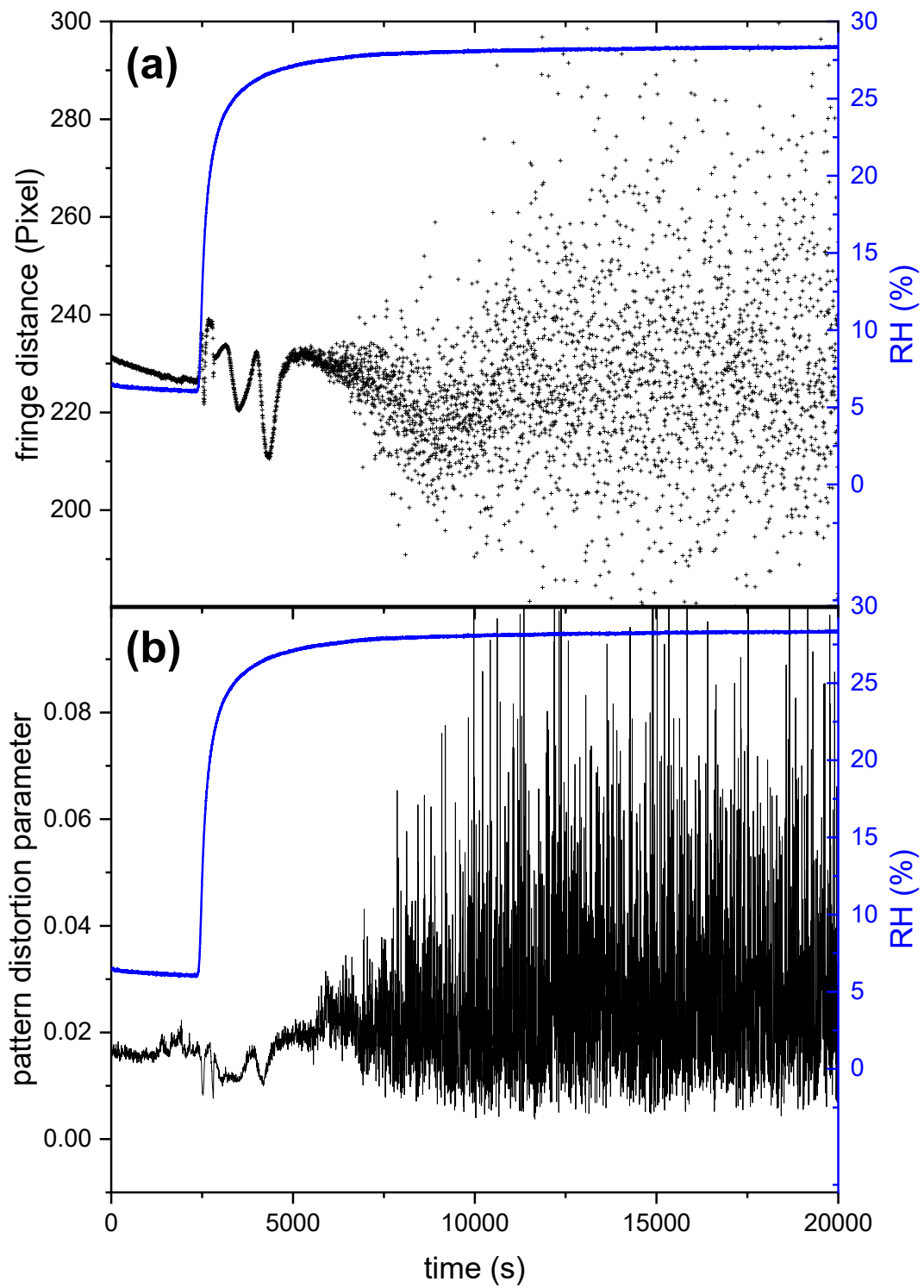


700

701 **Figure F-1: Mean fringe distance of AA particle exposed to UV up to 80% mass loss. While the fringe distance**
702 **oscillates with size change, TAOS pattern is clearly visible throughout the entire experiment, indicating the absence of**
703 **phase transition.**

704

705 **Appendix G. Mean fringe distance and pattern distortion parameter of AA particle exposed to UV and O₃ up to**
706 **26% mass loss upon humidifying**



708 **Figure G-1: (a) Mean fringe distance and (b) pattern distortion parameter of AA particle exposed to UV and O₃ up to**
709 **26% mass loss upon increasing RH from 6.0% to 28.4%. Significant increase in fluctuations in fringe distance (a) and**
710 **pattern distortion parameter (b) are observed at 6,000 s, indicating the efflorescence of AA.**

711
712 **Data availability.** All data of the figures are available online at <https://doi.org/10.3929/ethz-c-000788184>
713 (Antossian et al., 2025).

714
715 **Author contributions.** Funding was acquired by UKK. Experiments were conceptualized by UKK and CA and
716 carried out by CA. The data were analyzed by CA and UKK. The manuscript was written by CA and revised by
717 UKK and MM.

718
719 **Competing interests.** The authors declare that they have no conflict of interest.

720
721 **Disclaimer.**

722
723 **Acknowledgements.** The authors would like to thank Colette Heald for providing helpful feedback on the
724 manuscript. The authors would like to acknowledge Kristopher McNeill and Oleksandr Yushchenko for their
725 assistance in the absorbance measurements.

726
727 **Financial support.** This research has been supported by the Eidgenössische Technische Hochschule Zürich (grant
728 no. 23-1 ETH-020)

729
730 **Review statement.**

731
732 **References**

733 Antossian, C., Müller, M., and Krieger, U. K.: Photochemical and ozone-induced aging
734 significantly alter the viscosity of aqueous trans-aconitic acid aerosol particles (Data collection),
735 ETH Research Collection [dataset], doi: 10.3929/ethz-c-000788184, 2025.
736 Athanasiadis, A., Fitzgerald, C., Davidson, N. M., Giorio, C., Botchway, S. W., Ward, A. D.,
737 Kalberer, M., Pope, F. D., and Kuimova, M. K.: Dynamic viscosity mapping of the oxidation of
738 squalene aerosol particles, *Phys. Chem. Chem. Phys.*, 18, 30385-30393,
739 doi:10.1039/c6cp05674a, 2016.
740 Baboornian, V. J., Crescenzo, G., Huang, Y. Z., Mahrt, F., Shiraiwa, M., Bertram, A. K., and
741 Nizkorodov, S. A.: Sunlight can convert atmospheric aerosols into a glassy solid state and modify
742 their environmental impacts, *Proc. Natl. Acad. Sci. U. S. A.*, 119, 10, doi:
743 10.1073/pnas.2208121119, 2022.
744 Bastelberger, S., Krieger, U. K., Luo, B. P., and Peter, T.: Diffusivity measurements of volatile
745 organics in levitated viscous aerosol particles, *Atmos. Chem. Phys.*, 17, 8453-8471,
746 doi:10.5194/acp-17-8453-2017, 2017.
747 Bones, D. L., Reid, J. P., Lienhard, D. M., and Krieger, U. K.: Comparing the mechanism of water
748 condensation and evaporation in glassy aerosol, *Proc. Natl. Acad. Sci. U. S. A.*, 109, 11613-
749 11618, doi:10.1073/pnas.1200691109, 2012.

750 Braun, C. and Krieger, U. K.: Two dimensional angular light scattering in aqueous NaCl single
751 aerosol particles during deliquescence and efflorescence, *Opt. Express*, 8, 314-321,
752 doi:10.1364/oe.8.000314, 2001.

753 Bruni, G. O. and Klasson, K. T.: Aconitic Acid Recovery from Renewable Feedstock and Review of
754 Chemical and Biological Applications, *Foods*, 11, 18, doi:10.3390/foods11040573, 2022.

755 Chan, L. P. and Chan, C. K.: Roles of the Phase State and Water Content in Ozonolysis of Internal
756 Mixtures of Maleic Acid and Ammonium Sulfate Particles, *Aerosol Sci. Technol.*, 46, 781-793,
757 doi:10.1080/02786826.2012.665514, 2012.

758 Chan, M. N., Kreidenweis, S. M., and Chan, C. K.: Measurements of the hygroscopic and
759 deliquescence properties of organic compounds of different solubilities in water and their
760 relationship with cloud condensation nuclei activities, *Environ. Sci. Technol.*, 42, 3602-3608,
761 doi:10.1021/es7023252, 2008.

762 Chenyakin, Y., Ullmann, D. A., Evoy, E., Renbaum-Wolff, L., Kamal, S., and Bertram, A. K.:
763 Diffusion coefficients of organic molecules in sucrose-water solutions and comparison with
764 Stokes-Einstein predictions, *Atmos. Chem. Phys.*, 17, 2423-2435, doi:10.5194/acp-17-2423-
765 2017, 2017.

766 Cornard, J. P., Rasmiwetti, and Merlin, J. C.: Molecular structure and spectroscopic properties of
767 4-nitrocatechol at different pH: UV-visible, Raman, DFT and TD-DFT calculations, *Chem. Phys.*,
768 309, 239-249, doi: 10.1016/j.chemphys.2004.09.020, 2005.

769 Davies, J. F.: Mass, charge, and radius of droplets in a linear quadrupole electrodynamic
770 balance, *Aerosol Sci. Technol.*, 53, 309-320, doi:10.1080/02786826.2018.1559921, 2019.

771 Davis, E. J. and Periasamy, R.: LIGHT-SCATTERING AND AERODYNAMIC SIZE MEASUREMENTS
772 FOR HOMOGENEOUS AND INHOMOGENEOUS MICROSPHERES, *Langmuir*, 1, 373-379,
773 doi:10.1021/la00063a020, 1985.

774 Debenedetti, P. G. and Stillinger, F. H.: Supercooled liquids and the glass transition, *Nature*, 410,
775 259-267, doi:10.1038/35065704, 2001.

776 Dockery, D. W. and Pope, C. A.: ACUTE RESPIRATORY EFFECTS OF PARTICULATE AIR-
777 POLLUTION, *Annu. Rev. Public Health*, 15, 107-132, doi:10.1146/annurev.pu.15.050194.000543,
778 1994.

779 Dou, J., Alpert, P. A., Arroyo, P. C., Luo, B. P., Schneider, F., Xto, J., Huthwelker, T., Borca, C. N.,
780 Henzler, K. D., Raabe, J., Watts, B., Herrmann, H., Peter, T., Ammann, M., and Krieger, U. K.:
781 Photochemical degradation of iron(III) citrate/citric acid aerosol quantified with the combination
782 of three complementary experimental techniques and a kinetic process model, *Atmos. Chem.*
783 *Phys.*, 21, 315-338, doi:10.5194/acp-21-315-2021, 2021.

784 Duplissy, J., DeCarlo, P. F., Dommen, J., Alfarra, M. R., Metzger, A., Barmypadimos, I., Prevot, A. S.
785 H., Weingartner, E., Tritscher, T., Gysel, M., Aiken, A. C., Jimenez, J. L., Canagaratna, M. R.,
786 Worsnop, D. R., Collins, D. R., Tomlinson, J., and Baltensperger, U.: Relating hygroscopicity and
787 composition of organic aerosol particulate matter, *Atmos. Chem. Phys.*, 11, 1155-1165,
788 doi:10.5194/acp-11-1155-2011, 2011.

789 Einstein, A.: Über die von der molekularkinetischen Theorie der Wärme geforderte Bewegung von
790 in ruhenden Flüssigkeiten suspendierten Teilchen, *Ann. Phys.*, 17, 549-560, 1905.

791 Evoy, E., Kamal, S., Patey, G. N., Martin, S. T., and Bertram, A. K.: Unified Description of Diffusion
792 Coefficients from Small to Large Molecules in Organic-Water Mixtures, *J. Phys. Chem. A*, 124,
793 2301-2308, doi:10.1021/acs.jpca.9b11271, 2020.

794 Gou, Y. F., Xie, M. J., and Chen, J.: The phase state and viscosity of organic aerosol and related
795 impacts on atmospheric physicochemical processes: A review, *Atmos. Environ.*, 343, 17,
796 doi:10.1016/j.atmosenv.2024.120985, 2025.

797 Han, S., Hong, J., Luo, Q. W., Xu, H. B., Tan, H. B., Wang, Q. Q., Tao, J. C., Zhou, Y. Q., Peng, L., He,
798 Y., Shi, J. N., Ma, N., Cheng, Y. F., and Su, H.: Hygroscopicity of organic compounds as a function
799 of organic functionality, water solubility, molecular weight, and oxidation level, *Atmos. Chem.*
800 *Phys.*, 22, 3985-4004, doi:10.5194/acp-22-3985-2022, 2022.

801 Hildebrandt Ruiz, L., Paciga, A. L., Cerully, K. M., Nenes, A., Donahue, N. M., and Pandis, S. N.:
802 Formation and aging of secondary organic aerosol from toluene: changes in chemical
803 composition, volatility, and hygroscopicity, *Atmos. Chem. Phys.*, 15, 8301-8313,
804 doi:10.5194/acp-15-8301-2015, 2015.

805 Hosny, N. A., Fitzgerald, C., Vysniauskas, A., Athanasiadis, A., Berkemeier, T., Uygur, N., Pöschl,
806 U., Shiraiwa, M., Kalberer, M., Pope, F. D., and Kuimova, M. K.: Direct imaging of changes in
807 aerosol particle viscosity upon hydration and chemical aging, *Chem. Sci.*, 7, 1357-1367,
808 doi:10.1039/c5sc02959g, 2016.

809 Jakubczyk, D., Derkachov, G., Kolwas, M., and Kolwas, K.: Combining weighting and
810 scatterometry: Application to a levitated droplet of suspension, *J. Quant. Spectrosc. Radiat.*
811 *Transf.*, 126, 99-104, doi:10.1016/j.jqsrt.2012.11.010, 2013.

812 Jimenez, J. L., Canagaratna, M. R., Donahue, N. M., Prevot, A. S. H., Zhang, Q., Kroll, J. H.,
813 DeCarlo, P. F., Allan, J. D., Coe, H., Ng, N. L., Aiken, A. C., Docherty, K. S., Ulbrich, I. M., Grieshop,
814 A. P., Robinson, A. L., Duplissy, J., Smith, J. D., Wilson, K. R., Lanz, V. A., Hueglin, C., Sun, Y. L.,
815 Tian, J., Laaksonen, A., Raatikainen, T., Rautiainen, J., Vaattovaara, P., Ehn, M., Kulmala, M.,
816 Tomlinson, J. M., Collins, D. R., Cubison, M. J., Dunlea, E. J., Huffman, J. A., Onasch, T. B., Alfarra,
817 M. R., Williams, P. I., Bower, K., Kondo, Y., Schneider, J., Drewnick, F., Borrmann, S., Weimer, S.,
818 Demerjian, K., Salcedo, D., Cottrell, L., Griffin, R., Takami, A., Miyoshi, T., Hatakeyama, S.,
819 Shimono, A., Sun, J. Y., Zhang, Y. M., Dzepina, K., Kimmel, J. R., Sueper, D., Jayne, J. T., Herndon,
820 S. C., Trimborn, A. M., Williams, L. R., Wood, E. C., Middlebrook, A. M., Kolb, C. E., Baltensperger,
821 U., and Worsnop, D. R.: Evolution of Organic Aerosols in the Atmosphere, *Science*, 326, 1525-
822 1529, doi:10.1126/science.1180353, 2009.

823 Kalberer, M., Paulsen, D., Sax, M., Steinbacher, M., Dommen, J., Prevot, A. S. H., Fisseha, R.,
824 Weingartner, E., Frankevich, V., Zenobi, R., and Baltensperger, U.: Identification of polymers as
825 major components of atmospheric organic aerosols, *Science*, 303, 1659-1662,
826 doi:10.1126/science.1092185, 2004.

827 Kanakidou, M., Seinfeld, J. H., Pandis, S. N., Barnes, I., Dentener, F. J., Facchini, M. C., Van
828 Dingenen, R., Ervens, B., Nenes, A., Nielsen, C. J., Swietlicki, E., Putaud, J. P., Balkanski, Y., Fuzzi,
829 S., Horth, J., Moortgat, G. K., Winterhalter, R., Myhre, C. E. L., Tsigaridis, K., Vignati, E.,
830 Stephanou, E. G., and Wilson, J.: Organic aerosol and global climate modelling: a review, *Atmos.*
831 *Chem. Phys.*, 5, 1053-1123, doi:10.5194/acp-5-1053-2005, 2005.

832 Koop, T., Bookhold, J., Shiraiwa, M., and Pöschl, U.: Glass transition and phase state of organic
833 compounds: dependency on molecular properties and implications for secondary organic
834 aerosols in the atmosphere, *Phys. Chem. Chem. Phys.*, 13, 19238-19255,
835 doi:10.1039/c1cp22617g, 2011.

836 Krieger, U. K., Siegrist, F., Marcolli, C., Emanuelsson, E. U., Gobel, F. M., Bilde, M., Marsh, A.,
837 Reid, J. P., Huisman, A. J., Riipinen, I., Hyttinen, N., Mylly, N., Kurtén, T., Bannan, T., Percival, C.
838 J., and Topping, D.: A reference data set for validating vapor pressure measurement techniques:
839 homologous series of polyethylene glycols, *Atmos. Meas. Tech.*, 11, 49-63, doi:10.5194/amt-11-
840 49-2018, 2018.

841 Kroll, J. H. and Seinfeld, J. H.: Chemistry of secondary organic aerosol: Formation and evolution
842 of low-volatility organics in the atmosphere, *Atmos. Environ.*, 42, 3593-3624,
843 doi:10.1016/j.atmosenv.2008.01.003, 2008.

844 Kroll, J. H., Lim, C. Y., Kessler, S. H., and Wilson, K. R.: Heterogeneous Oxidation of Atmospheric
845 Organic Aerosol: Kinetics of Changes to the Amount and Oxidation State of Particle-Phase
846 Organic Carbon, *J. Phys. Chem. A*, 119, 10767-10783, doi:10.1021/acs.jpca.5b06946, 2015.

847 Kroll, J. H., Donahue, N. M., Jimenez, J. L., Kessler, S. H., Canagaratna, M. R., Wilson, K. R.,
848 Altieri, K. E., Mazzoleni, L. R., Wozniak, A. S., Bluhm, H., Mysak, E. R., Smith, J. D., Kolb, C. E.,
849 and Worsnop, D. R.: Carbon oxidation state as a metric for describing the chemistry of
850 atmospheric organic aerosol, *Nat. Chem.*, 3, 133-139, doi:10.1038/nchem.948, 2011.

851 Kuwata, M. and Martin, S. T.: Phase of atmospheric secondary organic material affects its
852 reactivity, *Proc. Natl. Acad. Sci. U. S. A.*, 109, 17354-17359, doi:10.1073/pnas.1209071109,
853 2012.

854 Lambe, A. T., Onasch, T. B., Massoli, P., Croasdale, D. R., Wright, J. P., Ahern, A. T., Williams, L. R.,
855 Worsnop, D. R., Brune, W. H., and Davidovits, P.: Laboratory studies of the chemical composition
856 and cloud condensation nuclei (CCN) activity of secondary organic aerosol (SOA) and oxidized
857 primary organic aerosol (OPOA), *Atmos. Chem. Phys.*, 11, 8913-8928, doi:10.5194/acp-11-8913-
858 2011, 2011.

859 Lienhard, D. M., Bones, D. L., Zuend, A., Krieger, U. K., Reid, J. P., and Peter, T.: Measurements of
860 Thermodynamic and Optical Properties of Selected Aqueous Organic and Organic-Inorganic
861 Mixtures of Atmospheric Relevance, *J. Phys. Chem. A*, 116, 9954-9968, doi:10.1021/jp3055872,
862 2012.

863 Marcolli, C. and Krieger, U. K.: Relevance of Particle Morphology for Atmospheric Aerosol
864 Processing, *Trends Chem.*, 2, 1-3, doi:10.1016/j.trechm.2019.11.008, 2020.

865 Marcolli, C., Luo, B. P., Peter, T., and Wienhold, F. G.: Internal mixing of the organic aerosol by gas
866 phase diffusion of semivolatile organic compounds, *Atmos. Chem. Phys.*, 4, 2593-2599,
867 doi:10.5194/acp-4-2593-2004, 2004.

868 Mu, Q., Shiraiwa, M., Octaviani, M., Ma, N., Ding, A. J., Su, H., Lammel, G., Pöschl, U., and
869 Cheng, Y. F.: Temperature effect on phase state and reactivity controls atmospheric multiphase
870 chemistry and transport of PAHs, *Sci. Adv.*, 4, 8, doi:10.1126/sciadv.aap7314, 2018.

871 Muller, G. T. A. and Stokes, R. H.: THE MOBILITY OF THE UNDISSOCIATED CITRIC ACID
872 MOLECULE IN AQUEOUS SOLUTION, *Transactions of the Faraday Society*, 53, 642-645,
873 doi:10.1039/tf9575300642, 1957.

874 Müller, M., Mishra, A., Berkemeier, T., Hausammann, E., Peter, T., and Krieger, U. K.:
875 Electrodynamic balance-mass spectrometry reveals impact of oxidant concentration on product
876 composition in the ozonolysis of oleic acid, *Phys. Chem. Chem. Phys.*, 24, 27086-27104,
877 doi:10.1039/d2cp03289a, 2022.

878 Murray, B. J., Wilson, T. W., Dobbie, S., Cui, Z. Q., Al-Jumur, S., Möhler, O., Schnaiter, M., Wagner,
879 R., Benz, S., Niemand, M., Saathoff, H., Ebert, V., Wagner, S., and Kärcher, B.: Heterogeneous
880 nucleation of ice particles on glassy aerosols under cirrus conditions, *Nat. Geosci.*, 3, 233-237,
881 doi:10.1038/ngeo817, 2010.

882 Nel, A.: Air pollution-related illness: Effects of particles, *Science*, 308, 804-806,
883 doi:10.1126/science.1108752, 2005.

884 O'Brien, R. E. and Kroll, J. H.: Photolytic Aging of Secondary Organic Aerosol: Evidence for a
885 Substantial Photo-Recalcitrant Fraction, *J. Phys. Chem. Lett.*, 10, 4003-4009,
886 doi:10.1021/acs.jpcllett.9b01417, 2019.

887 O'Meara, S., Topping, D. O., and McFiggans, G.: The rate of equilibration of viscous aerosol
888 particles, *Atmos. Chem. Phys.*, 16, 5299-5313, doi:10.5194/acp-16-5299-2016, 2016.

889 Pang, X. F.: *Water: Molecular Structure and Properties*, World Scientific Publishing Co. Pte. Ltd.,
890 doi:10.1142/8669, 2014.

891 Pankow, J. F.: AN ABSORPTION-MODEL OF THE GAS AEROSOL PARTITIONING INVOLVED IN THE
892 FORMATION OF SECONDARY ORGANIC AEROSOL, *Atmos. Environ.*, 28, 189-193,
893 doi:10.1016/1352-2310(94)90094-9, 1994.

894 Petters, M. D. and Kreidenweis, S. M.: A single parameter representation of hygroscopic growth
895 and cloud condensation nucleus activity, *Atmos. Chem. Phys.*, 7, 1961-1971, doi:10.5194/acp-7-
896 1961-2007, 2007.

897 Pope, F. D., Gallimore, P. J., Fuller, S. J., Cox, R. A., and Kalberer, M.: Ozonolysis of Maleic Acid
898 Aerosols: Effect upon Aerosol Hygroscopicity, Phase and Mass, *Environ. Sci. Technol.*, 44, 6656-
899 6660, doi:10.1021/es1008278, 2010.

900 Pöschl, U. and Shiraiwa, M.: Multiphase Chemistry at the Atmosphere-Biosphere Interface
901 Influencing Climate and Public Health in the Anthropocene, *Chem. Rev.*, 115, 4440-4475,
902 doi:10.1021/cr500487s, 2015.

903 Price, H. C., Mattsson, J., Zhang, Y., Bertram, A. K., Davies, J. F., Grayson, J. W., Martin, S. T.,
904 O'Sullivan, D., Reid, J. P., Rickards, A. M. J., and Murray, B. J.: Water diffusion in atmospherically
905 relevant α -pinene secondary organic material, *Chem. Sci.*, 6, 4876-4883,
906 doi:10.1039/c5sc00685f, 2015.

907 Rickards, A. M. J., Miles, R. E. H., Davies, J. F., Marshall, F. H., and Reid, J. P.: Measurements of
908 the Sensitivity of Aerosol Hygroscopicity and the κ Parameter to the O/C Ratio, *J. Phys. Chem. A*,
909 117, 14120-14131, doi:10.1021/jp407991n, 2013.

910 Rickards, A. M. J., Song, Y. C., Miles, R. E. H., Preston, T. C., and Reid, J. P.: Variabilities and
911 uncertainties in characterising water transport kinetics in glassy and ultraviscous aerosol, *Phys.*
912 *Chem. Chem. Phys.*, 17, 10059-10073, doi:10.1039/c4cp05383d, 2015.

913 Romonosky, D. E., Laskin, A., Laskin, J., and Nizkorodov, S. A.: High-Resolution Mass
914 Spectrometry and Molecular Characterization of Aqueous Photochemistry Products of Common
915 Types of Secondary Organic Aerosols, *J. Phys. Chem. A*, 119, 2594-2606, doi:10.1021/jp509476r,
916 2015.

917 Rothfuss, N. E. and Petters, M. D.: Influence of Functional Groups on the Viscosity of Organic
918 Aerosol, *Environ. Sci. Technol.*, 51, 271-279, doi:10.1021/acs.est.6b04478, 2017.

919 Saito, S., Numadate, N., Teraoka, H., Enami, S., Kobayashi, H., and Hama, T.: Impurity
920 contribution to ultraviolet absorption of saturated fatty acids, *Sci. Adv.*, 9, 7,
921 doi:10.1126/sciadv.adj6438, 2023.

922 Seinfeld, J. H. and Pandis, S. N.: Atmospheric chemistry and physics: from air pollution to
923 climate change, Third Edition, John Wiley & Sons, Inc., ISBN: 9781119221166, 2016.

924 Shiraiwa, M., Ammann, M., Koop, T., and Pöschl, U.: Gas uptake and chemical aging of semisolid
925 organic aerosol particles, *Proc. Natl. Acad. Sci. U. S. A.*, 108, 11003-11008,
926 doi:10.1073/pnas.1103045108, 2011.

927 Shrivastava, M., Lou, S., Zelenyuk, A., Easter, R. C., Corley, R. A., Thrall, B. D., Rasch, P. J., Fast, J.
928 D., Simonich, S. L. M., Shen, H. Z., and Tao, S.: Global long-range transport and lung cancer risk
929 from polycyclic aromatic hydrocarbons shielded by coatings of organic aerosol, *Proc. Natl.*
930 *Acad. Sci. U. S. A.*, 114, 1246-1251, doi:10.1073/pnas.1618475114, 2017.

931 Song, Y. C., Haddrell, A. E., Bzdek, B. R., Reid, J. P., Barman, T., Topping, D. O., Percival, C., and
932 Cai, C.: Measurements and Predictions of Binary Component Aerosol Particle Viscosity, *J. Phys.*
933 *Chem. A*, 120, 8123-8137, doi:10.1021/acs.jpca.6b07835, 2016.

934 Steimer, S. S., Krieger, U. K., Te, Y. F., Lienhard, D. M., Huisman, A. J., Luo, B. P., Ammann, M., and
935 Peter, T.: Electrodynamic balance measurements of thermodynamic, kinetic, and optical aerosol
936 properties inaccessible to bulk methods, *Atmos. Meas. Tech.*, 8, 2397-2408, doi:10.5194/amt-8-
937 2397-2015, 2015.

938 Steiner, B., Berge, B., Gausmann, R., Rohmann, J., and Rühl, E.: Fast in situ sizing technique for
939 single levitated liquid aerosols, *Appl. Optics*, 38, 1523-1529, doi:10.1364/ao.38.001523, 1999.

940 Sun, M. R. and Smith, G. D.: Photolytic Mass Loss of Humic Substances Measured with a Quartz
941 Crystal Microbalance, *ACS Earth Space Chem.*, 8, 1623-1633,
942 doi:10.1021/acsearthspacechem.4c00134, 2024.

943 Willis, M. D. and Wilson, K. R.: Coupled Interfacial and Bulk Kinetics Govern the Timescales of
944 Multiphase Ozonolysis Reactions, *J. Phys. Chem. A*, 126, 4991-5010,
945 doi:10.1021/acs.jpca.2c03059, 2022.

946 Wolf, M. J., Zhang, Y., Zawadowicz, M. A., Goodell, M., Froyd, K., Freney, E., Sellegri, K., Rösch,
947 M., Cui, T. Q., Winter, M., Lacher, L., Axisa, D., DeMott, P. J., Levin, E. J. T., Gute, E., Abbatt, J.,
948 Koss, A., Kroll, J. H., Surratt, J. D., and Cziczo, D. J.: A biogenic secondary organic aerosol source
949 of cirrus ice nucleating particles, *Nat. Commun.*, 11, 9, doi:10.1038/s41467-020-18424-6, 2020.

950 Zardini, A. A., Krieger, U. K., and Marcolli, C.: White light Mie resonance spectroscopy used to
951 measure very low vapor pressures of substances in aqueous solution aerosol particles, *Opt.*
952 *Express*, 14, 6951-6962, doi:10.1364/oe.14.006951, 2006.

953 Zardini, A. A., Sjogren, S., Marcolli, C., Krieger, U. K., Gysel, M., Weingartner, E., Baltensperger,
954 U., and Peter, T.: A combined particle trap/HTDMA hygroscopicity study of mixed

955 inorganic/organic aerosol particles, *Atmos. Chem. Phys.*, 8, 5589-5601, doi:10.5194/acp-8-
956 5589-2008, 2008.

957 Zaveri, R. A., Easter, R. C., Shilling, J. E., and Seinfeld, J. H.: Modeling kinetic partitioning of
958 secondary organic aerosol and size distribution dynamics: representing effects of volatility,
959 phase state, and particle-phase reaction, *Atmos. Chem. Phys.*, 14, 5153-5181, doi:10.5194/acp-
960 14-5153-2014, 2014.

961 Zelenyuk, A., Imre, D., Beránek, J., Abramson, E., Wilson, J., and Shrivastava, M.: Synergy
962 between Secondary Organic Aerosols and Long-Range Transport of Polycyclic Aromatic
963 Hydrocarbons, *Environ. Sci. Technol.*, 46, 12459-12466, doi:10.1021/es302743z, 2012.

964 Zhang, Q., Jimenez, J. L., Canagaratna, M. R., Allan, J. D., Coe, H., Ulbrich, I., Alfarra, M. R.,
965 Takami, A., Middlebrook, A. M., Sun, Y. L., Dzepina, K., Dunlea, E., Docherty, K., DeCarlo, P. F.,
966 Salcedo, D., Onasch, T., Jayne, J. T., Miyoshi, T., Shimonono, A., Hatakeyama, S., Takegawa, N.,
967 Kondo, Y., Schneider, J., Drewnick, F., Borrmann, S., Weimer, S., Demerjian, K., Williams, P.,
968 Bower, K., Bahreini, R., Cottrell, L., Griffin, R. J., Rautiainen, J., Sun, J. Y., Zhang, Y. M., and
969 Worsnop, D. R.: Ubiquity and dominance of oxygenated species in organic aerosols in
970 anthropogenically-influenced Northern Hemisphere midlatitudes, *Geophys. Res. Lett.*, 34, 6,
971 doi:10.1029/2007gl029979, 2007.

972 Zobrist, B., Soonsin, V., Luo, B. P., Krieger, U. K., Marcolli, C., Peter, T., and Koop, T.: Ultra-slow
973 water diffusion in aqueous sucrose glasses, *Phys. Chem. Chem. Phys.*, 13, 3514-3526,
974 doi:10.1039/c0cp01273d, 2011.

975 Zuend, A., Marcolli, C., Luo, B. P., and Peter, T.: A thermodynamic model of mixed organic-
976 inorganic aerosols to predict activity coefficients, *Atmos. Chem. Phys.*, 8, 4559-4593,
977 doi:10.5194/acp-8-4559-2008, 2008.

978 Zuend, A., Marcolli, C., Booth, A. M., Lienhard, D. M., Soonsin, V., Krieger, U. K., Topping, D. O.,
979 McFiggans, G., Peter, T., and Seinfeld, J. H.: New and extended parameterization of the
980 thermodynamic model AIOMFAC: calculation of activity coefficients for organic-inorganic
981 mixtures containing carboxyl, hydroxyl, carbonyl, ether, ester, alkenyl, alkyl, and aromatic
982 functional groups, *Atmos. Chem. Phys.*, 11, 9155-9206, doi:10.5194/acp-11-9155-2011, 2011.

983

984